A Proper Orthogonal Decomposition (POD) method for the prediction of fan-OGV broadband interaction noise

Xiaowan Liu *, Paruchuri Chaitanya † and Phillip Joseph ‡
University of Southampton, SO17 1BJ, Southampton, UK

The turbulent wakes generated by a rotor interacting with outlet guide vanes (OGVs) is one of the dominant broadband noise sources in a turbofan engine. An accurate representation of the rotor wake turbulence is therefore important for the reliable prediction of the rotor-OGV interaction noise. This paper presents a turbulence synthesis method based on a spectral Proper Orthogonal Decomposition (POD) representation of the turbulent wake that aims to reproduce the desired velocity cross-spectrum along the OGV leading edges where noise is emitted due to turbulence-OGVs interaction. The method is first developed in the frequency domain based on a superposition of vortical modes with the appropriate amplitudes. Fourier modes and POD modes are proposed to represent the two-point velocity spectrum. The POD modes will be shown to be highly efficient in reconstructing the flow field near the tip region where a large-scale coherent structure is present. An extension of the POD synthetic turbulence method to the time domain is also presented by means of a white noise filtering technique to allow the generation of time varying velocity signals with the desired cross spectral characteristics. The results show that both the one- and two-point statistics can be closely reproduced. The proposed frequency-domain POD synthetic turbulence method for fan broadband noise prediction for a realistic fan-OGV configuration is illustrated by the use of a frequency-domain linearised Navier-Stokes solver to predict the sound power radiation due to each vortical mode. Overall sound power levels at a number of discrete frequencies are predicted and compared against measured noise data. Agreement is found to be within the uncertainty of the noise sound power measurement.

Nomenclature

c_0 = speed of sound

f = frequency

Presented as Paper AIAA 2021-2164 at AIAA AVIATION 2021 FORUM, VIRTUAL EVENT, 2-6 August, 2021
*Research fellow, Xiaowan.Liu@soton.ac.uk
†Lecturer, C.C.Paruchuri@soton.ac.uk
‡Professor, Senior member AIAA, pfj@isvr.soton.ac.uk

I	=	acoustic intensity
k	=	turbulence kinetic energy or Tayler and Sofrin scatter index
$l_\theta(\omega), l_r(\omega)$	=	length scale spectrum in the $\theta-$, $r-$direction
L_w	=	wake width
m	=	incident vortical mode order in the azimuthal direction
n	=	incident vortical mode order in the radial direction
p	=	acoustic pressure field
$R()$	=	correlation function
S	=	surface area
$S()$	=	auto spectrum
t	=	time
u_x, u_θ, u_r	=	velocity disturbance in the $x-$, $\theta-$ and $r-$direction
u_n	=	upwash velocity component
U_x, U_θ, U_r	=	mean velocity in the $x-$, $\theta-$ and $r-$direction
U_c	=	convection velocity
V	=	number of outlet guide vanes
W	=	sound power
x, θ, r	=	cylindrical coordinates in the annular duct
α, β	=	axial, azimuthal wavenumber of incident vortical disturbance
γ	=	coherence function
$\delta()$	=	Dirac delta function
δ_{ij}	=	Kronecker delta
η	=	radiation efficiency
λ_{mn}	=	eigenvalue of cross spectral matrix C_m
Λ	=	integral length scale
μ	=	scattered acoustic mode order in the azimuthal direction
ν	=	scattered acoustic mode order in the radial direction
ρ_0	=	density
ρ	=	correlation coefficient
τ_c	=	integral time scale
ϕ_{mn}	=	vortical modal function of order (m, n)
$\psi_{mn,\mu\nu}$	=	acoustic modal function of order (μ, ν) associated with the incident vortical mode (m, n)

ω = angular frequency

Superscripts

$*$ = complex conjugate

$\pm$ = upstream/downstream propagating acoustic waves

$\hat{}$ = modal amplitude

$\bar{}$ = spatial average

I. Introduction

THE broadband noise due to the interaction between the turbulence in the wake from the rotor with the downstream Outlet Guide Vanes (OGV) is one of the major components of noise from an aircraft engine, especially at approach conditions. Broadband fan noise has been studied extensively, theoretically and experimentally as well using numerical Computational Fluid Dynamic prediction methods. Current analytical methods are nearly all restricted to simple idealised geometries, such as flat plates at zero-incidence situated within highly idealised mean flow profiles [1–5]. A number of highly detailed noise and flow measurements have also been made on engines but these are usually done at laboratory-scale where the flow conditions do not precisely match those in a full-scale engine [6, 7]. A comprehensive study regarding the impact of different assumptions made in the analytical models on noise predictions can be found in [8].

A. Critical comparison of CFD-based methods for fan broadband noise predictions

Numerical simulations have also been attempted mainly based on hybrid approaches that separate the computation of the sound sources from the propagation.

1. LES/LBM with acoustic analogy

This approach emphasises on a direct computation of the sound sources through high-fidelity unsteady simulations, such as Large Eddy Simulation (LES), Improved Delayed Detached Eddy Simulation (IDDES, a hybrid RANS-LES method) or Lattice Boltzmann Method (LBM), and the sound propagation to far-field is given by a Green's function using acoustic analogy. The use of high-fidelity numerical simulations allows to resolve turbulence scales over a wide frequency range as long as the mesh is sufficiently fine. This helps to improve broadband noise prediction accuracy, but results in high computational cost.

Only few CFD studies have performed high-fidelity simulations to solve the fan/OGV system and analyse the fan broadband noise [9–15]. Table. 1 shows the computational configuration and cost in these simulations. The CPU time corresponds to the wall clock time multiplied by the number of CPUs used. Only Suzuki et al. [10] and Casalino et al. [14] used a computational domain covering full stage (22 fan blades and 54 OGVs over the whole azimuthal direction)

with nacelle geometry included. Comparing Casalino et al. [14] and Arroyo et al. [12], it is clear that the LBM-based method is much more time efficient, although the CPU performance in the two studies are different.

Table 1 Computational configuration and cost in high-fidelity simulations for fan broadband noise prediction

	Engine	CFD method	CFD domain	Cells (in million)	CPU time (in hour)
Suzuki et al. [10]	NASA SDT	IDDES	full annular	140	
Casalino et al. [14] (fine mesh)	NASA SDT	LBM	full annular	136	60,480 for 10 revolutions
Arroyo et al. [12]	NASA SDT	wall-modelled LES	1/11 annular	75	1,080,000 for 13 revolutions
Kholodov and Moreau [13]	NASA SDT	wall-modelled LES	1/22 annular (fan only)	62	
Lewis et al. [11]	ACAT1	wall-modelled LES	1/20 annular	95	

A significant challenge associated with this hybrid method is that the Green's function is only known for canonical cases assuming free-field, uniform flow, annular cylindrical ducts. The extension to slowly varying ducts, lined ducts, mean swirling flows is possible but complex. Neglecting their effects in the wave propagation might have an impact on the accuracy of the method. Lewis et al. [11] and Arroyo et al. [12] conducted comparisons of two acoustic analogies, the Ffowcs Williams-Hawkings (FW-H) free field analogy and the Goldstein's duct analogy, by coupling with LES. They found that one based on Goldstein's analogy gives better prediction since it allows to include the duct propagation effect.

Instead of using the OGV's surface as the source integration surface, as those done in [11, 12], Suzuki et al. [10] and Casalino et al. [14] applied permeable FW-H surfaces outside the duct enclosing the nacelle. This avoids the need of a tailored Green's function to take account of the duct propagation effect, but it requires the grid resolution to be sufficiently fine in the whole computational domain to propagate the sound waves to the FW-H integration surface, which will lead to a significant increase in the computational cost. In addition, particular attention has to be paid to the design of the permeable FW-H surfaces to avoid the generation of spurious noise due to vortical disturbance exiting the downstream end of the surface.

2. LEE/LNS with synthetic turbulence model

Another approach based on the Linearised Euler (LEE) or Navier-Stokes (LNS) equations coupled with a synthetic turbulence inflow can also be considered, which is the focus of the present paper. In this approach, a turbulent field is synthesised based on statistical properties obtained from CFD method and injected as source term to the LEE/LNS. The problem is therefore simplified to the study of the noise due to the vorticity-leading edge interaction; the noise generation and propagation can be obtained from the solutions of the LEE/LNS equations. By injecting the synthetic turbulence through inlet, the LEE/LNS computational domain can be reduced to include the stators only, which helps to

reduce the computational cost.

A number of studies have modelled leading-edge noise generation and propagation by solving the linearised equations in frequency domain [16–18] or in time domain [19–22]. The frequency domain method has shown to be efficient in predicting the tonal noise and is also possible to be applied to analyse the broadband noise at discrete frequencies. The time domain method has the advantage that the continuous noise spectrum can be predicted within a single simulation, but tends to be more prone to numerical instability for 3D simulations [23, 24].

An accurate representation of the wake turbulence is essential for the accurate interaction noise predictions, and therefore, the choice of a synthetic turbulence method might have an impact on the prediction accuracy. The synthetic turbulence methods used in CAA solvers include the Fourier-mode based methods, the Random Particle Mesh (RPM) method, and the Synthetic Eddy Method (SEM). The advantages and disadvantages of different synthetic methods are summarised in Table 2 which also includes the mesh requirement. The references shown in Table 2 are focused on the application in aeroacoustic fields. In addition to these synthetic methods, it is also possible to obtain turbulence data through a high-fidelity simulation, e.g. LES or LBM, which is also included in Table 2 for comparison. A more detailed introduction of each synthetic turbulence method is provided in the subsequent section.

Most existing studies for turbulence synthesis have been conducted with the assumption of homogeneous flows, which are not well suited to represent the turbulence generated within the rotor wake which exhibits strong span-wise inhomogeneity. In this paper, a Proper Orthogonal Decomposition (POD) based synthetic turbulence method is investigated for the representation of inhomogeneous turbulence. The advantages of the POD method over the Fourier method for inhomogeneous turbulent flows have been shown by Glegg and Devenport [25] who described the use of POD in solving the problem of turbulent flow interaction with rigid surfaces. The present paper is essentially an extension of paper [25] by coupling the POD-based synthetic turbulence method with a frequency domain LNS solver to predict the turbulence-OGV interaction noise in a hard walled duct containing the sheared and swirling flows encountered in the engine interstage. This paper also includes an extension of this POD-based method to time domain, which is expected to be useful for turbulence synthesis in the time domain Euler solver.

B. Synthetic turbulence methods

1. Fourier-mode based method

The Fourier-mode based method for turbulence synthesis was first introduced by Kraichnan [26] to study the diffusion of fluid particles where the synthetic turbulent velocity field was constructed through a discrete sum of Fourier modes with randomly chosen amplitudes, wavenumbers and phase. This approach was further developed by Karweit et al. [27] and Bechara et al. [28] for Computational Aeroacoustics (CAA) application in relation to jet noise modelling, which is known as stochastic noise generation and radiation (SNGR) approach. In [27, 28], the velocity amplitude at each wavenumber was specified from the prescribed energy spectrum. In [28], Bechara et al. also introduced temporal

Table 2 Comparison of different turbulence generation methods.

Method	Governing equation	Mesh requirements	Turbulence resolving	Advantages	Disadvantages	References
LBM	BGK Boltzmann equation	15 points per acoustic wavelength [14]	Yes	Unified method includes both wake turbulence and noise prediction	High cost but more efficient than LES	Casalino et al. [14], Grace et al. [32]
Fourier method	Coupled with CAA solver	10 points per wavelength [21]	No	Explicitly reproducing the desired spectrum; easy to achieve divergence-free	Not efficient to represent the cross-spectral matrix for inhomogeneous flows	Polascek et al. [21], Chaitanya et al. [30], Blazquez and Corral [31]
RPM	Coupled with CAA solver	11 points per eddy radius [33]	No	Explicitly reproducing the desired correlations; easy to incorporate source convection at locally varying speed	Limited work on inhomogeneous flows	Ewert [34], Dieste and Gabard [19], Kissner and Guérin [23], Gea-Aguilera et al. [33], Wohlbrandt et al. [20]
SEM	Coupled with CAA solver	10 points per eddy radius [35]	No	Efficient and easy to implement	Complicated to choose the location and the size of an individual eddy	Jarrin et al. [36], Sescu and Hixon [37], Kim and Haeri [35]
POD	Coupled with CAA solver		No	Capable of identifying large-scale coherent structures; most efficient in representing inhomogeneous flows	Large number of POD modes to represent small scale turbulence	None

correlation into the synthesized turbulence field through filtering the random time series using a Gaussian filter in the frequency domain. Another method to include the time dependence into the turbulence statistics was proposed by Bailly and Juvé [29] by introducing a constant convection velocity in the formulation similar to that due to Kraichnan. In the SNGR, the divergence-free constraint (for incompressible flow) can be readily imposed by expressing the amplitude vectors as the cross product of randomly chosen vectors with the wavenumber vectors. This method is therefore highly suitable for use in CAA applications as the divergence-free constraint is important to avoid the generation of acoustic waves as part of the synthetic turbulence generation. Previously, Chaitanya et al. [30] demonstrated the prediction of turbulence-cascade interaction noise in 2D using a Fourier mode decomposition of the incoming turbulence. No span-wise correlation effects were therefore included in the 2D approach. This 2D calculation is then applied to a number of 'strips' across the span of the OGV whose width is greater than turbulence integral length scale. The total sound power is then computed from the sum of powers from each strip. A significant deficiency with this approach is that the correct two-point statistics along the span are absent, which are known to cause an increase in predicted noise at low frequencies, with relatively small difference at higher frequencies [4] (greater than BPF). A high sensitivity of the noise results to the number of strips has been reported by Blázquez-Navarro and Corral [31] who combined the strip-based approach with a frequency domain LNS solver to investigate the fan blockage effect on the upstream transmission of turbulence-OGV interaction noise.

2. Random particle mesh method

Another widely used stochastic approach for generating synthetic turbulence is the digital filter method whose aim is to filter random signals to reproduce the spatial and temporal correlations of the turbulent field. The filter function can be specified based on a given correlation function. An early attempt using the filter-based technique can be found in Klein et al. [38] for generating inflow turbulence in LES simulations of turbulent jet flows.

A significant extension of the filter-based technique for CAA applications was made by Ewert [34], now known as the RPM method. In the RPM, a fluctuating stream function is generated through spatially filtering a white noise field and the convection property is introduced by solving the convection equations of the white noise field. This approach allows the inclusion of both frozen turbulence and evolving turbulence. By expressing the velocity fluctuations in terms of a stream function, the RPM approach allows the generation of strictly divergence-free flow fields. Ewert et al. [39] applied this approach to study a variety of aeroacoustic problems, including trailing-edge noise, slat noise and jet noise. Kissner and Guérin [23] investigated fan broadband noise by coupling the RPM method with 3D PErturbed Nonconservative nonlinear Euler equations.

The filter function used in [34, 39] is Gaussian which has been shown to be efficient for multi-dimensional problem and can closely approximate the correlations for the case of homogeneous turbulence. Dieste and Gabard [19] used the RPM with non-Gaussian filters in order to generate different idealised energy spectra, such as Liepmann and Von

Kármán spectra. They also investigated the effect of frozen turbulence and evolving turbulence and found that the results are similar in these two cases. Other filter functions, based on superposition of Gaussian filters with different length scales and amplitudes, have been investigated in [40, 41].

3. Synthetic eddy method

Another method used in fan broadband noise predictions is the SEM proposed by Jarrin et al. [36] based on the assumption that turbulence can be considered as a superposition of randomly distributed eddies. The eddies are injected through inlet boundary and are assumed to be convected with the mean flow using Taylor's frozen turbulence hypothesis. Proper choice of shape functions to represent the eddies is important for reproducing the spatial and temporal correlations in the SEM. The shape functions can be either a Gaussian, a Mexican hat wavelet, a Morlet mother wavelet, or a combination of them. Based on the SEM method, Sescu and Hixon [37] developed a low-noise synthetic turbulent inflow condition for aeroacoustic calculations. To ensure a clean aeroacoustic environment, they imposed two constraints on the synthetic flow field. One is the divergence-free condition which was achieved by means of a vector potential and the other is to ensure the shape functions satisfy the convection equations. Kim and Haeri [35] applied the low-noise model of Sescu and Hixon to a three-dimensional (3D) simulation of aerofoil-turbulence interaction noise. In order to reproduce Von Kármán velocity spectra, Kim and Haeri [35] introduced 15 constraint parameters to control and optimise the overall distribution of random eddies. Gea-Aguilera et al. [33] developed an advanced digital filter method by making use of the favourable aspects of the RPM and SEM methods. The energy spectrum can be obtained by superposition of Gaussian filters with different amplitudes and length scales. This approach has shown good results in 2D computation of turbulence-cascade interaction noise by coupling with a time-domain LEE solver [42]. An extension of this approach to account for anisotropic turbulence effect can be found in [43].

4. POD method

Procedures based on Proper Orthogonal Decomposition of the turbulent flow can also be applied to synthesise turbulent fields once the two-point velocity statistics are available. Only few studies have been performed using this approach and they are limited to incompressible flows. Perret et al. [44] presented an inflow turbulence generation method by interpolating and extrapolating experimental data onto numerical method based on the use of POD in the time domain. It should be noted that the POD method used in their study, referred to as snapshot POD, only generates spatial modes and the modal coefficients do not contain temporal correlation information. However, the present study employs a spectral POD method, specifically the POD decomposition of the two-point velocity cross spectral matrix at discrete frequencies, which has been shown in [45] to be able to describe space-time evolution of coherent structures.

This paper presents a theoretical framework for predicting fan broadband interaction noise based on a proper orthogonal decomposition of the circumferentially-averaged rotor wake two-point turbulence velocity statistics. These

two-points velocity statistics in the direction normal to the blade provides a complete description of the rotor wake turbulence necessary for fan broadband noise calculations [46].

This paper is organized as follows: Section II describes different modal basis functions (Fourier modes and POD modes) for synthesising the two point statistics of the rotor wake turbulence at any arbitrary frequency. The frequency-domain POD method is then extended in Section III to the time domain. In Section IV validation of the method is illustrated in the frequency domain through the reconstruction of a 'target' velocity cross-spectrum based on the turbulence characteristics obtained from RANS solutions. In Section V the reconstruction efficiency and accuracy are investigated for the POD and Fourier modes. Section V also includes the assessment of the time domain reconstruction for the one- and two-point statistics. In Section VI the proposed frequency-domain POD method is then applied to predict the fan broadband interaction noise measured in a model-scale transonic fan rig. Finally the critique of the POD method for fan broadband noise prediction are summarised in Section VII.

II. Frequency-domain turbulence synthesis method

Turbulence generated within the rotor wake convects from the spinning rotor along a helical path towards the OGV, which then scatters into noise at their leading edges. The turbulence in the wake can be generally regarded as frozen along this helical path. It has been shown that the time-averaged (over many shaft rotations) noise spectrum can be related to the time-averaged velocity cross-spectrum in the stationary reference frame [1]. In this reference frame the two-point velocity statistics are cyclo-stationary, i.e., they vary periodically at the blade passing frequency.

Consider the frequency spectrum $u(r, \theta, \omega)$ of the turbulent velocity component normal to the OGV leading edge over the r-θ plane of the OGV leading edge (where r and θ are respectively in the radial and azimuthal direction). Note that the Fourier transform with respect to time needed to obtain $u(r, \theta, \omega)$ from the instantaneous velocity $u(r, \theta, t)$ must be taken over a time much longer than the period of rotation of the rotor. The instantaneous velocity must be periodic in the azimuthal θ direction and therefore $u(r, \theta, \omega)$ can be decomposed into its azimuthal modal components $u_m(r, \omega)$,

$$u(r, \theta, \omega) = \sum_{m}^{\infty} u_m(r, \omega) e^{im\theta}. \tag{1}$$

Fan broadband noise at any particular frequency is completely determined by the velocity cross-spectrum C of the upwash velocity u between any two locations (r, θ) and (r', θ') defined by:

$$C(r, \theta, r', \theta', \omega) = \lim_{T \to \infty} \frac{1}{T} E\left[u(r, \theta, \omega) u^*(r', \theta', \omega)\right], \tag{2}$$

where the operator E [] denotes the expectation or ensemble average.

Substituting $\theta' = \theta - \Delta\theta$ and Eq. 1 into Eq. 2 gives

$$C(r,\theta,r',\theta',\omega) = \lim_{T\to\infty}\left\{\frac{1}{T}\sum_{m}^{\infty}\sum_{m'}^{\infty} E\left[u_m(r,\omega)u^*_{m'}(r',\omega)\right] e^{i(m-m')\theta} e^{im'\Delta\theta}\right\}. \tag{3}$$

Since $u(r,\theta,\omega)$ represents the averaged velocity spectrum over many rotations, the velocity cross-spectrum $C(r,\theta,r',\theta',\omega)$ must be homogeneous in the $\theta-$direction and hence independent of θ. This condition applied to Eq. 3 suggests that $m = m'$, which yields the cross-spectrum in the $\theta-$direction as only a function of $\Delta\theta = \theta - \theta'$, i.e.,

$$C(r,r',\Delta\theta,\omega) = \sum_{m=-\infty}^{\infty} C_m(r,r',\omega)e^{im\Delta\theta}, \tag{4}$$

where C_m is the radial cross-spectrum associated with the m^{th} azimuthal mode,

$$C_m(r,r',\omega) = \lim_{T\to\infty}\left\{\frac{1}{T}E\left[u_m(r,\omega)u^*_m(r',\omega)\right]\right\}. \tag{5}$$

Each azimuthal modal velocity component $u_m(r,\omega)$ in Eq. 5 can be expressed as a sum of radial vortical modes $\phi_{mn}(r,\omega)$ of amplitude $\hat{u}_{mn}(\omega)$ of the form,

$$u_m(r,\omega) = \sum_{n}^{\infty}\hat{u}_{mn}(\omega)\phi_{mn}(r,\omega), \tag{6}$$

where $\phi_{mn}(r,\omega)$ are arbitrary mode shape functions. Different choices of mode functions, such as POD modes and Fourier modes, are discussed below. However, in this paper we mainly focus on POD modes by virtue of providing the most efficient representation of the cross-spectrum for inhomogeneous flows [25].

In practice the modal sum of Eq. 6 is approximated by a finite sum of N radial modes, which at each azimuthal mode order m and each frequency ω, can then be expressed in the matrix form,

$$\mathbf{u}_m = \mathbf{\Phi}_m\hat{\mathbf{u}}_m, \tag{7}$$

where $\mathbf{u}_m$ is a vector of velocities at L discrete radial positions,

$$\mathbf{u}_m = \left[u_m(r_1,\omega)\ u_m(r_2,\omega)\ u_m(r_3,\omega)\ \cdots\ u_m(r_L,\omega)\right]^{\mathrm{T}}, \tag{8}$$

and $\hat{\mathbf{u}}_m$ is a vector of mode amplitudes up to radial mode order N,

$$\hat{\mathbf{u}}_m = \left[\hat{u}_{m1}(\omega)\ \hat{u}_{m2}(\omega)\ \hat{u}_{m3}(\omega)\cdots\hat{u}_{mN}(\omega)\right]^{\mathrm{T}}, \tag{9}$$

and $\mathbf{\Phi}_m$ is a matrix whose columns are the mode shape functions at a given frequency ω,

$$\mathbf{\Phi}_m = \begin{bmatrix} | & | & & | \\ \phi_{m1}(r,\omega) & \phi_{m2}(r,\omega) & \cdots & \phi_{mN}(r,\omega) \\ | & | & & | \end{bmatrix}. \tag{10}$$

Substituting Eq. 6 into Eq. 5, the radial cross-spectrum C_m can be expressed in the matrix form,

$$\mathbf{C}_m = \mathbf{\Phi}_m \hat{\mathbf{C}}_m \mathbf{\Phi}_m^{\mathrm{H}}, \tag{11}$$

where the subscript H denotes the Hermitian transpose. The cross-spectral amplitude matrix is given by,

$$\hat{\mathbf{C}}_m = \lim_{T\to\infty} \left\{ \frac{1}{T} E\left[\hat{\mathbf{u}}_m \hat{\mathbf{u}}_m^{\mathrm{H}} \right] \right\}. \tag{12}$$

Our objective now is to determine the cross-spectral amplitude matrix $\hat{\mathbf{C}}_m$ associated with the choice of mode functions $\mathbf{\Phi}_m$ at each azimuthal mode order m and frequency ω that provides the least squares fit to the target cross-spectral matrix $\mathbf{C}_m$.

A. Different choices of mode functions

1. POD modes

Proper Orthogonal Decomposition provides the set of basis functions or modes that best represents, in a least squares sense, a given flow field (e.g. velocity) with the least number of modes. The POD was introduced in the context of turbulence by Lumley [47] and has been widely used as a technique to extract coherent structures from turbulent flow fields. There are a number of variants of POD. A spectral POD method [48] is applied in the present study as it is capable of describing space-time evolution of coherent structures.

At a single frequency the optimal set of POD modes in Eq. 7 is obtained by maximising the averaged projection of the velocity vector $\mathbf{u}_m$ onto the mode function $\mathbf{\Phi}_m$, i.e.,

$$\underset{\mathbf{\Phi}_m}{\operatorname{argmax}} \frac{E\left[|(\mathbf{u}_m, \mathbf{\Phi}_m)|^2 \right]}{\|\mathbf{\Phi}_m\|^2}. \tag{13}$$

A necessary condition for Eq. 13 to be valid is that $\mathbf{\Phi}_m$ is the eigenfunctions of the cross-spectrum $\mathbf{C}_m$,

$$\mathbf{C}_m \mathbf{\Phi}_m = \mathbf{\Phi}_m \mathbf{\Lambda}_m, \tag{14}$$

where the columns of $\mathbf{\Phi}_m$ represent the POD modes at L discrete radial locations (Here since $\mathbf{C}_m$ is a square matrix, so the number of modes is equal to the number of radial locations), and where $\mathbf{\Lambda}_m$ is the diagonal matrix

of corresponding eigenvalues. The eigenmodes, or POD modes, are normally ranked according to their eigenvalues, $\lambda_1 \geq \lambda_2 \geq \cdots \geq 0$. The number of modes that are needed for the spectral reconstruction will be assessed in Section V.A where the use of POD modes to identify the large-scale coherent structures are also investigated.

Since the cross-spectral matrix $\mathbf{C}_m$ is Hermitian, it can be shown that the eigenvalues are real and the eigenvectors are mutually orthogonal, i.e., $E\left[\mathbf{\Phi}_m \mathbf{\Phi}_m^{\mathrm{H}}\right] = \mathbf{I}$, so that,

$$\mathbf{C}_m = \mathbf{\Phi}_m \mathbf{\Lambda}_m \mathbf{\Phi}_m^{\mathrm{H}}. \tag{15}$$

Comparing Eq. 15 with Eq. 11 suggests that the eigenvalue matrix corresponds to the cross-spectral amplitude matrix, $\hat{\mathbf{C}}_m = \mathbf{\Lambda}_m$, which can be expanded as,

$$E\left[\hat{u}_{mn}(\omega)\hat{u}^*_{mn'}(\omega)\right] = \delta_{nn'}\lambda_{mn}(\omega). \tag{16}$$

The above result implies that the modal amplitudes $\hat{u}_{mn}$ are uncorrelated between different radial modes within the same azimuthal mode and frequency. This property will be shown below to be useful as means of simplifying the calculation of total radiated sound power.

2. Fourier modes

The radial mode functions ϕ_{mn} in Eq. 6 may also be expressed in terms of Fourier modes,

$$\phi_{mn}(r, \omega) = e^{ik_r r}, \tag{17}$$

where the n^{th} radial wavenumber component is given by $k_r = \frac{2\pi n}{r_t - r_h}$ in which r_t and r_h indicate the radius at the tip and hub respectively.

For homogeneous flows, in which the two-point correlation is only a function of the separation distance $C(r, r') = C(r - r')$, the Fourier modes correspond exactly to the eigenmodes of the cross-spectral matrix $\mathbf{C}_m$, while the cross-spectral amplitude matrix corresponds to the eigenvalue matrix as shown in Eq. 16. The proof of this identity can be found in [49]. This paper focuses on the turbulence generated within the rotor wake which exhibits strong span-wise inhomogeneity. In such cases the Fourier modes are no longer the eigenmodes of $\mathbf{C}_m$ and the mode amplitudes $\hat{\mathbf{u}}_m$ in Eq. 7 that minimises E defined by,

$$E = \left\|\mathbf{u}_m - \mathbf{\Phi}_m \hat{\mathbf{u}}_m\right\|^2. \tag{18}$$

This condition is equivalent to projecting the velocity vector $\mathbf{u}_m$ onto the mode function $\mathbf{\Phi}_m$. The vector of mode amplitudes that gives the least error E, i.e. $\frac{\partial E}{\partial \hat{\mathbf{u}}_m} = 0$ is given by [50],

$$\hat{\mathbf{u}}_m = \mathbf{\Phi}_m^{+}\mathbf{u}_m, \tag{19}$$

where $\mathbf{\Phi}_m^{+} = (\mathbf{\Phi}_m^{\mathrm{H}}\mathbf{\Phi}_m)^{-1}\mathbf{\Phi}_m^{\mathrm{H}}$ is the pseudo inverse of $\mathbf{\Phi}_m$.

The optimum cross-spectral matrix of mode amplitudes $\hat{\mathbf{C}}_m$ in Eq. 12 may therefore be written as,

$$\hat{\mathbf{C}}_m = \mathbf{\Phi}_m^{+}\mathbf{C}_m\mathbf{\Phi}_m^{+\mathrm{H}}. \tag{20}$$

Note that $\hat{\mathbf{C}}_m$ obtained from the above result is no longer a diagonal matrix, unlike that in Eq. 16 for POD modes, as the Fourier modes are not, in general, the eigenmodes of the cross-spectrum $\mathbf{C}_m$ for inhomogeneous flows.

III. Synthetic turbulence method extended to the time domain

The frequency-domain POD method described above is now extended to synthesise the velocity signals in the time domain by making use of a filter-based method. The objective now is to synthesis the time domain velocity signals at every point over the $r-\theta$ plane $u(r,\theta,t)$ that has the desired two-point cross-spectrum of Eq. 2. The two-point cross-spectrum is modelled in this study using turbulent characteristics obtained from RANS. The details will be introduced in Section IV.

In general the time varying turbulence velocity signals $u(r,\theta,t)$ distributed over the cross section of the duct, are generated by filtering a white noise fields $x(r',\theta',t)$ and may be expressed as [34, 39],

$$u(r,\theta,t) = \int\int\int G(r,r',\theta-\theta',t-t')x(r',\theta',t')dr'd\theta'dt', \tag{21}$$

where $G(r,r',\theta-\theta',t-t')$ defines a 3D filter which contains both spatial and temporal correlation information. The white noise fields have the statistical properties: $E\left[x(r',\theta',t')\right] = 0$ and $E\left[x(r',\theta',t')x(r'+\Delta r',\theta'+\Delta\theta'+\Delta t')\right] = \delta(\Delta r')\delta(\Delta\theta')\delta(\Delta t')$. The filter is expressed as a function of the separation distance in the θ-direction and in time since the rotor wake turbulence is periodic in θ and t. However, the turbulence is inhomogeneous in the r-direction (as shown later), the filter is therefore expressed in the form $G(r,r',\theta-\theta',t-t')$ to represent the variation as a function of the input at r'. The expression in Eq. 21 is similar to the RPM [34], but the temporal correlation is controlled by the filter G, instead of solving a convection equation for the white noise field to impose the correct temporal correlation function. Furthermore, in the RPM method, the quantity generated from the convolution is a stream function and the fluctuating velocity can be expressed in terms of the stream function to satisfy the divergence-free constraint. In the present study, the divergence-free constraint is considered only in the frequency domain which is described in Appendix A.

Noting that the Fourier transform of the convolution of two functions is the product of their transforms, Eq. 21 can

then be written in terms of its Fourier transform pair with respect to θ and t,

$$u_m(r,\omega) = \int G_m(r,r',\omega)x_m(r',\omega)dr'. \tag{22}$$

In the numerical implementation of the filter the continuous integral equation (22) can be approximated through a finite sum [34],

$$u_m(r,\omega) = \sum_n^N G_{mn}(r,\omega)x_{mn}(\omega). \tag{23}$$

Eq. 23 can be interpreted as N source elements located at discrete radial points r_n contributing to the resulting velocity field. Here $G_{mn}(r,\omega) = G_m(r,r_n,\omega)$ and $x_{mn}(\omega) = \bar{x}_m(r_n,\omega)\Delta r_n$ where $\bar{x}_m(r_n,\omega) = \frac{1}{\Delta r}\int x_m(r_n,\omega)dr_n$ is the average of the white noise field over Δr_n.

Substituting Eq. 23 into Eq. 5 gives,

$$C_m(r,r',\omega) = \lim_{T\to\infty}\left\{\frac{1}{T}\sum_n\sum_{n'} G_{mn}(r,\omega)G^*_{mn'}(r',\omega)E\left[x_{mn}(\omega)x^*_{mn'}(\omega)\right]\right\}. \tag{24}$$

Since x is a white noise signal,

$$\lim_{T\to\infty}\left\{\frac{1}{T}E\left[x_{mn}(\omega)x^*_{mn'}(\omega)\right]\right\} = \sigma^2_{mn}\int\int\delta(r_n - r_{n'})dr_n dr_{n'} = \begin{Bmatrix} 0, & \text{if } n \neq n' \\ \sigma^2_{mn}\Delta r_n, & \text{if } n = n' \end{Bmatrix}, \tag{25}$$

where σ^2_{mn} is the mean square velocity per unit frequency in the span element Δr_n.

Thus, Eq. 24 becomes,

$$C_m(r,r',\omega) = \sum_n \Delta r_n\sigma^2_{mn}G_{mn}(r,\omega)G^*_{mn}(r',\omega). \tag{26}$$

From Eq. 5 and Eq. 6, we have

$$C_m(r,r',\omega) = \lim_{T\to\infty}\left\{\frac{1}{T}\sum_{n'}\sum_n E\left[\hat{u}_{mn}(\omega)\hat{u}^*_{mn'}(\omega)\right]\phi_{mn}(r,\omega)\phi^*_{mn'}(r',\omega)\right\}. \tag{27}$$

Equating Eq. 26 and Eq. 27 for C_m and using the property Eq. 16 for the POD modes,

$$G_{mn}(r,\omega) = \frac{\sqrt{\lambda_{mn}(\omega)}}{\sigma_{mn}\sqrt{\Delta r_n}}\phi_{mn}(r,\omega). \tag{28}$$

This result provides an explicit relationship between the time-domain filter and the POD modes. The modal shape ϕ_{mn} corresponding to the filter shape while the filter strength is controlled by the modal 'energy' λ_{mn}. It is worth mentioning that for the Fourier method (and the flow is inhomogeneous) or the RPM method using Gaussian filter, the

double sum in Eq. 27 must hold and the amplitude of the filter cannot be directly obtained as in Eq. 28. This has been shown in Gea-Aguilera et al. [33] where the amplitudes were determined through an optimisation process. The random velocity field can be synthesised by,

$$u(r,\theta,t) = \sum_{n}^{N} \text{IFFT}\left\{G_{mn}(r,\omega)x_{mn}(\omega)\right\}. \tag{29}$$

where IFFT indicates 2D inverse Fourier transform with respect to m and ω. The above expression is equivalent to $\sum_n^N G(r,r_n,\theta,t) * x(r_n,\theta,t)$ where $*$ denotes 2D convolution operation with respect to θ and t. Note that this method of generating the time domain velocity signals is preferred to pure convolution in the time domain $u(r,\theta,t) = G_n(r,\theta,t) * x_n(\theta,t)$ since convolution methods obtained using the DFT assume circular convolution which leads to spurious peaks in the frequency spectrum $u(r,\theta,\omega)$.

IV. Modelling of velocity cross-spectra of rotor wake

In this section we outline how the target velocity cross-spectrum used to validate the synthetic turbulence method may be estimated from the RANS solutions of the flow field over the OGV leading edge plane. However, we emphasise that more accurate cross-spectrum are generally required for accurate fan broadband noise calculations obtained from either from Hot-wire measurements or high fidelity time-resolved CFD such as LES [9–13] or LBM [14, 32].

A. RANS modelling of turbulence characteristics

RANS simulations are performed on the AneCom AeroTest Rotor1 (ACAT1) fan at approach condition. The ACAT1 fan has 20 rotor blades and 44 vanes. The RANS solver used in the present study is the Rolls-Royce *plc* code, HYDRA. The computational domain is limited to a single passage including fan, OGV and ESS blades as shown in Fig. 1. A mixing plane is used at the interface between the rotating fan and the fixed OGV domain to exchange of the steady flow data. The turbulence model applied is the $k-\omega$ SST model [51]. For brevity, the detailed grid configurations are not described here, which can be found in [52].

The turbulence characteristics are extracted at the plane aligned with the leading edge of the OGV as highlighted in Fig. 1. The contour plots of the axial mean velocity and the turbulence intensity downstream of the rotor are shown in Fig 2(a) and (b) respectively. The turbulence intensity is obtained from $\sqrt{\frac{2k}{3(U_x^2+U_\theta^2)}}$ where k is the turbulence kinetic energy (TKE) and U_x and U_θ are the axial and azimuthal mean velocity components, respectively. A secondary tip flow is clearly observed in Fig. 2. This feature will be shown to be important in the turbulence synthesis procedure. The turbulence characteristics in terms of the turbulence length scale and the circumferentially averaged turbulence intensity along the radius are shown in Fig. 3. The turbulence integral length-scale Λ is computed from the wake width as suggested by Jurdic et al. [53]: $\Lambda = 0.21L_w$, where L_w is the wake width defined as the width at half the maximum

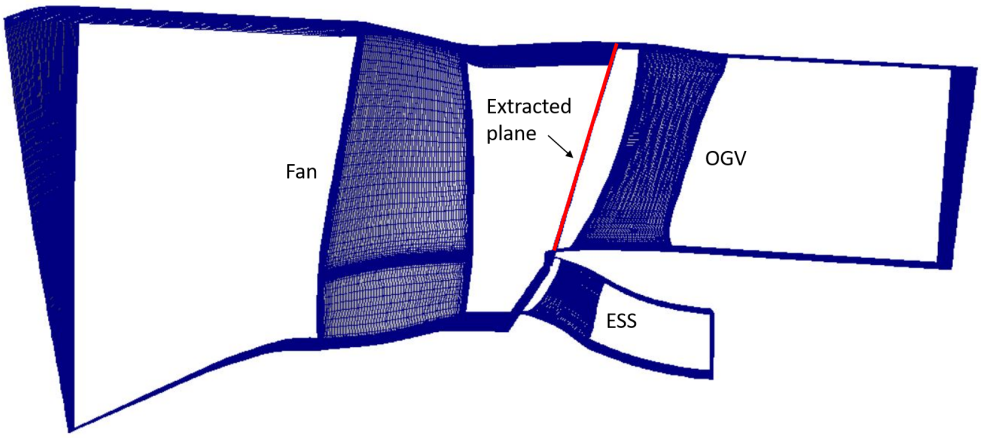

Fig. 1 Computational domain with the extraction plane highlighted.

velocity deficit. This finding is in close agreement with the classical results from Ganz et al. [6]. A comparison study of the length scale estimated using Jurdic's method with that from other definition methods as well as measurements can be found in [54]. The radial locations are normalised by the distance a between the tip and hub radii, with $r/a = 1$ corresponding to the tip and $r/a = 0$ the hub. These two quantities are found to vary dramatically near the tip, indicating strong span-wise inhomogeneity.

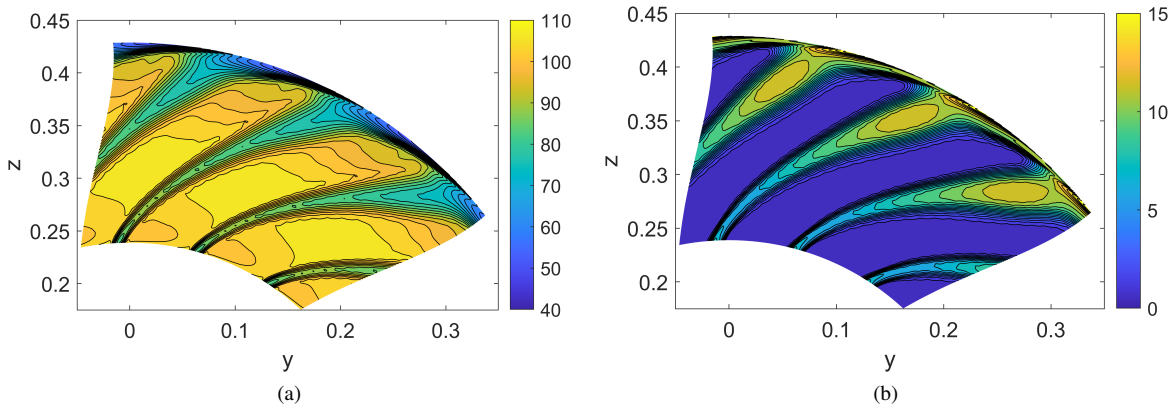

Fig. 2 (a) Mean axial velocity (m/s) and (b) turbulence intensity (%) contours at the extracted plane.

B. Target velocity cross-spectra

The turbulence characteristics extracted from the RANS solution in the above section are now used to construct the cross-spectrum of the upwash velocity component between all points along the OGV leading edge. Assuming homogeneity in the $\theta-$direction and statistical stationarity in time, the cross-spectrum can be expressed as a function of $\Delta\theta$ as shown in Eq. 3 and 4.

The turbulence statistics of turbulence intensities and length scales were found to vary considerably along the

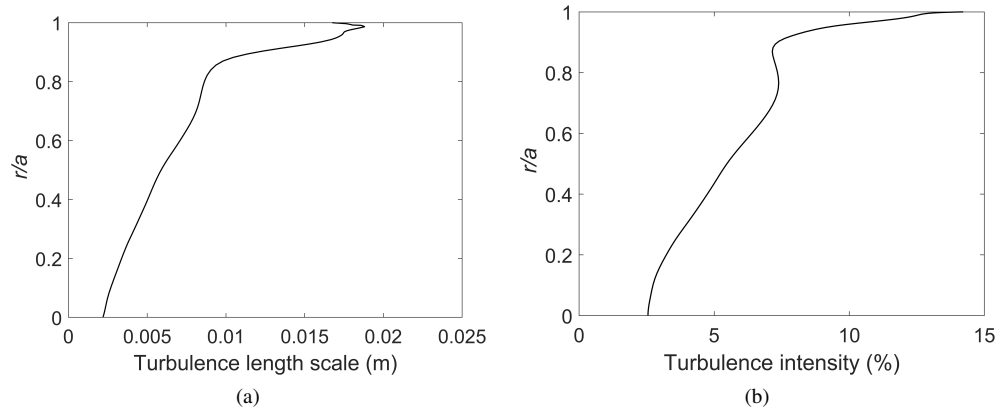

Fig. 3 Variations of circumferentially averaged (a) turbulence length scale and (b) turbulence intensity with radius.

span, especially near the tip (shown in Fig. 3). The radial variations in these statistical quantities are included when determining the turbulent energy and length scale spectra. For simplicity, we assume that the turbulence in the $r-$direction is locally homogeneous and the cross-spectrum with radial separation distance follows a Gaussian function. The velocity cross-spectrum between two locations (r, θ) and (r', θ') may be expressed as,

$$C(r, r', \Delta\theta, \omega) = \sqrt{S(r, \omega)S(r', \omega)}\gamma(l_\theta(\omega), l_r(\omega), r - r', r(\Delta\theta)), \tag{30}$$

where S is the auto-spectrum of the turbulent fluctuations which can be expressed as a von Kármán or Liepmann spectrum and γ is the coherence function, which we assume is of the form of a Gaussian function given by,

$$\gamma(l_\theta(\omega), l_r(\omega), r - r', r(\Delta\theta)) = e^{-\frac{r-r'}{l_r(\omega)}} e^{-\frac{r(\Delta\theta)}{l_\theta(\omega)}}, \tag{31}$$

where $l_r(\omega)$ and $l_\theta(\omega)$ are the length-scale spectrum in the radial and azimuthal directions, respectively, which can be determined from von Kármán or Liepmann spectrum as shown in [1]. However, for simplicity, we assume local isotropy and hence $l_r(\omega) = l_\theta(\omega)$.

Taking the Fourier transform of Eq. 30 with respect to $\Delta\theta$, we obtain the radial cross-spectrum associated with the m^{th} azimuthal mode,

$$C_m(r, r', \omega) = \frac{1}{2\pi}\int_{-\infty}^{\infty} C(r, r', \Delta\theta, \omega)e^{-im\Delta\theta}d\Delta\theta. \tag{32}$$

The velocity cross-spectral matrices obtained through Eq. 30−32 using von Kármán spectrum for $m = 0$ (corresponding to the circumferentially average) and 40 at three representative frequencies 400, 2000 and 4000 Hz are shown in Fig. 4. The results are normalised by the maximum value of the spectral matrix. Little variations are found between $m = 0$ and 40 except that the small-scale structures near the hub $(r/a = 0)$ seem to be more significant

for $m = 40$. A large-scale coherent structure is clearly observed near the tip ($r/a = 1$) at $f = 400$ Hz, indicative of a separated secondary tip flow that has been identified in Fig. 3. As the frequency increases the flow structures become smaller and tend to become evenly spread across the radius. This phenomenon is explained by the combined effect of the energy cross-spectrum and the coherence function which are shown in Fig. 5. As the locations move from near the tip ($r/a = 1$ and 0.98) to near the centre ($r/a = 0.7$ and 0.68), the energy level increases at frequencies above 1000 Hz and decreases below 1000 Hz. A similar trend is also found for the coherence variation. The frequency of the coherence peak increase from about 400 Hz to 2000 Hz as the locations move from $r/a = 1$ and 0.98 to $r/a = 0.7$ and 0.68, with a slight decrease in the peak coherence value from 0.9 to 0.8.

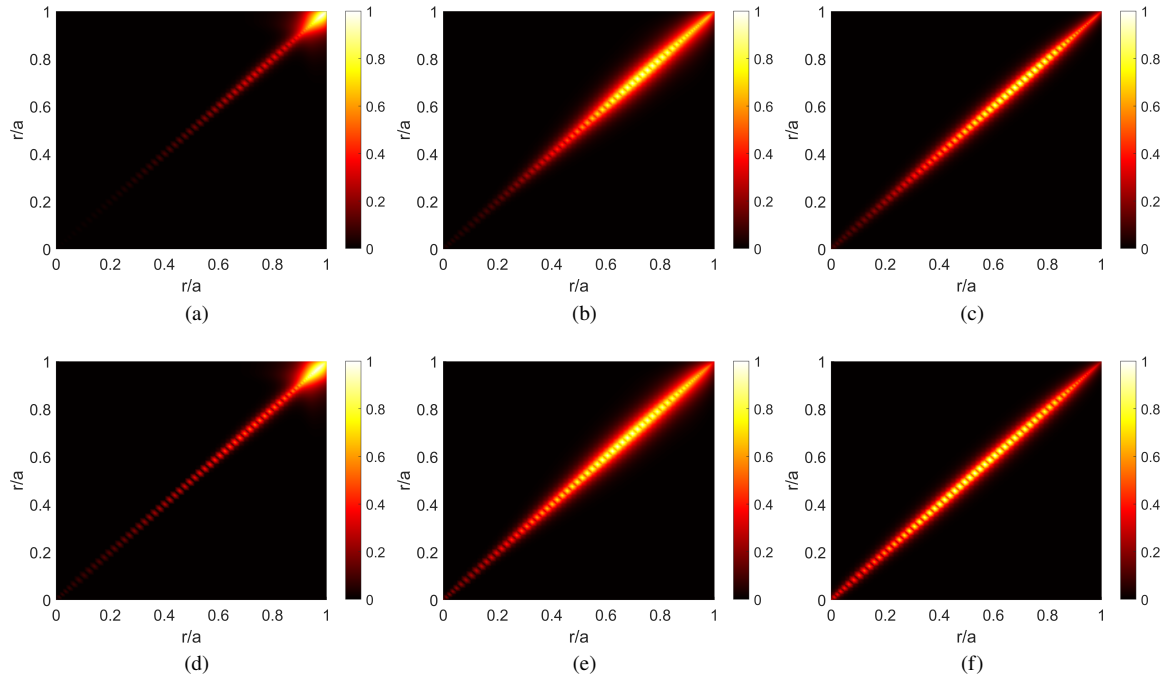

Fig. 4 Actual velocity cross-spectral matrix for (a) $m = 0$ and $f = 400$ Hz, (b) $m = 0$ and $f = 2000$ Hz, (c) $m = 0$ and $f = 4000$ Hz, (d) $m = 40$ and $f = 400$ Hz, (e) $m = 40$ and $f = 2000$ Hz, (f) $m = 40$ and $f = 4000$ Hz.

V. Reconstruction results

A. Frequency domain

In this section, both the POD modes and Fourier modes are investigated for their accuracy in reconstructing the target velocity cross-spectra in the frequency domain. A detailed analysis of the reconstruction efficiency is conducted for the POD modes. The reconstruction effectiveness of the Fourier modes is also assessed and compared with that of the POD modes.

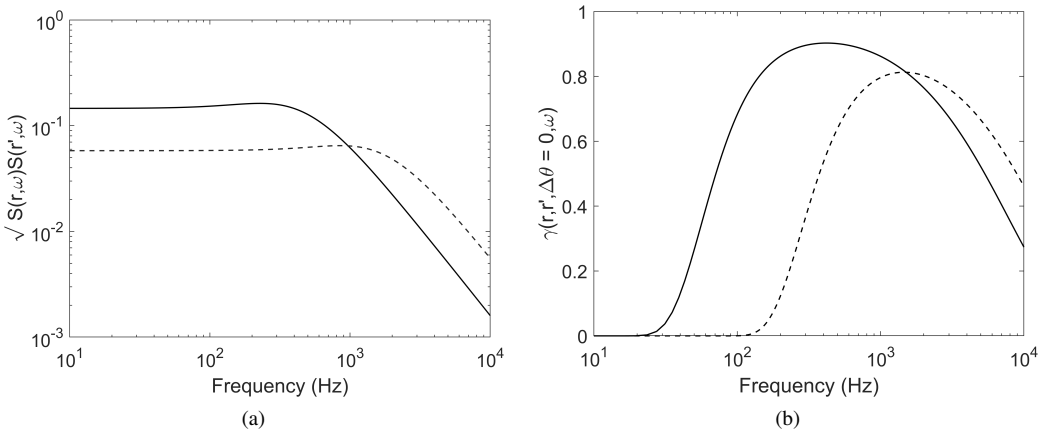

Fig. 5 (a) Energy cross-spectra and (b) coherence functions between radial points at (——) r/a = 1 and 0.98 and (- - -) r/a = 0.7 and 0.68.

1. POD modes

The 'energy' contained within each POD mode is represented by its eigenvalue, as indicated in Eq. 16, with the most energetic modes having the largest eigenvalues. The eigenvalue frequency spectra for different radial POD modes from 1 to 10 at the azimuthal mode order $m = 0$ are shown in Fig. 6(a). The first mode is seen to be the most energetic, particularly around 400 Hz, which can be explained by the presence of a large-scale coherent structure near the tip at this frequency (see Fig. 4(a)). At higher frequencies above 2000 Hz, smaller scale structures are observed, and thus the dominance of the first POD mode become less significant. The 'energy' contained in each POD mode as a fraction of the total 'energy' is shown in Fig. 6(b). The total energy, λ_{total}, is calculated by the incoherent sum over all eigenvalues. The first mode is found to contain about 57% of the total energy at 400 Hz, and this percentage reduces to about 11% at 4000 Hz.

Figure. 7 shows the energy spectra of the first three POD modes for the azimuthal mode orders m = 0, 20, 40 and 60. The eigenvalues are found to decrease slowly with m with negligible variations at frequencies above 2000 Hz. The eigenvalue distributions over m at 400 and 2000 Hz are shown in Fig. 8. Within each m mode, the contributions of the first four POD modes are presented. The dominance of the first POD mode is seen for different m although this dominance is less significant at higher m values. The variations of λ_{mn} with m can be seen to follow a Gaussian shape. This is simply a consequence of assuming a Gaussian coherence in the θ-direction (Eq. 31). In addition, the eigenvalues appear to decrease more slowly with m at 2000 Hz. This could be explained by the smaller length scale used at this frequency, as shown in Fig. 9 where the length-scale spectra were obtained from the von Kármán spectrum as in [1].

The fraction of the total energy reconstructed based on different numbers of POD modes is shown in Fig 10. Results are presented in terms of the ratio of truncated modal energy to the total energy as a function of frequency. Different azimuthal mode orders m = 0, 20, 40 and 60 are investigated. The efficiency of energy recovery is found to be highly

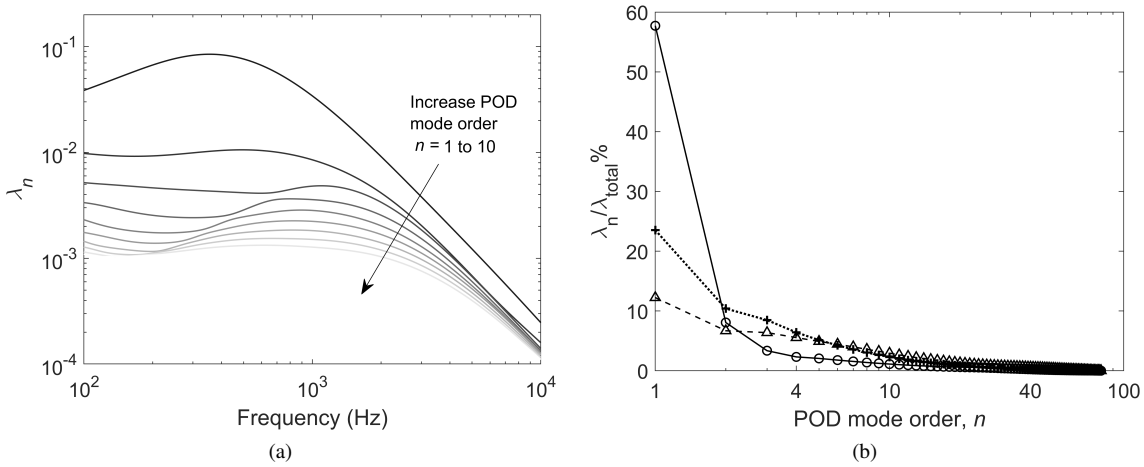

Fig. 6 (a) Eigenvalue spectra as a function of frequency for the first 10 POD modes at $m = 0$; (b) relative energy of each POD mode in percentage of the total energy for $m = 0$ at frequencies: (——○) 400 Hz, (·····+) 2000 Hz and (- - -△) 4000 Hz..

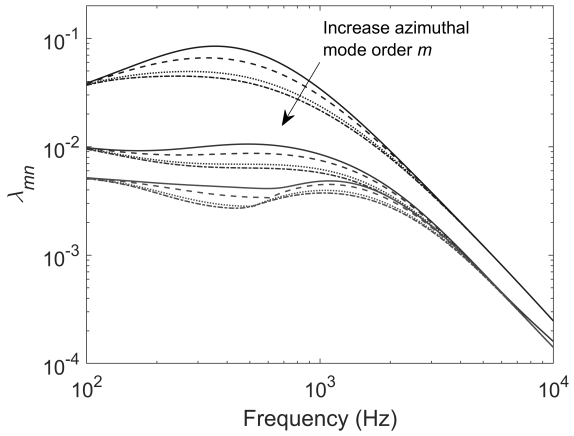

Fig. 7 Eigenvalue spectra of the first three POD modes for different m: (——) $m = 0$, (- - -) $m = 20$, (·····) $m = 40$ and (-·-·-) $m = 60$.

dependent on frequency. Using the first 10 POD modes is able to recover nearly 80% of the total energy at frequencies around 400 Hz, but less than 50% is recovered above 4000 Hz. However, we emphasise that that some vortical modes are more efficient in radiating sound power than others. The radiation efficiency of the modes will be addressed in Section VI. Also shown in Fig. 10 is that varying the azimuthal mode order has only slight effect on energy recovery, especially when more than 10 POD modes are used.

Fig. 11 shows the modal contributions of the POD mode 1, 2, 3 and 10 to the cross-spectral matrix at $m = 0$ and frequencies 400, 2000 and 4000 Hz. The individual contribution is plotted by calculating the cross-spectrum using a single POD mode. For example, for mode $n = 1$, this is expressed as,

$$C_1(r, r', \omega) = \lambda_1(\omega)\phi_1(r, \omega)\phi_1^*(r', \omega). \tag{33}$$

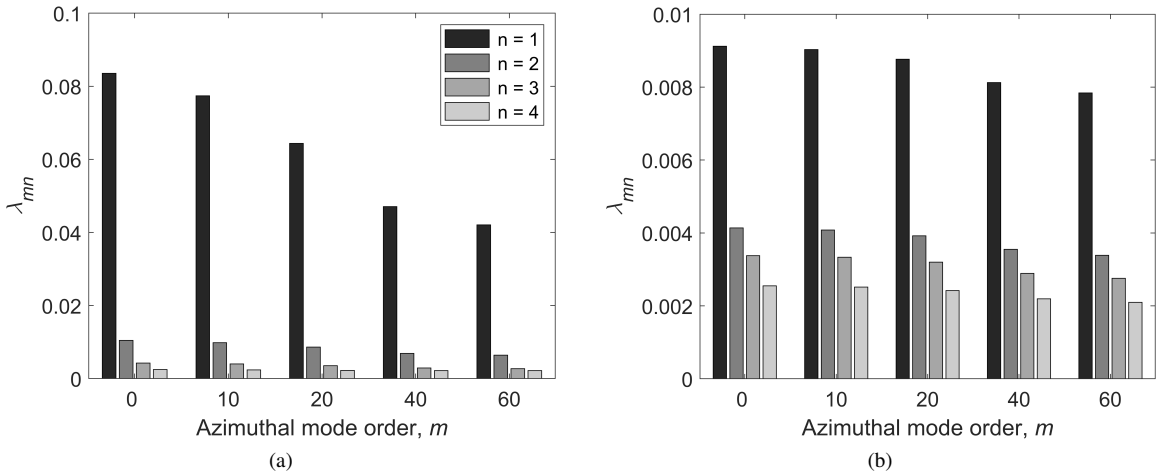

Fig. 8 Eigenvalue spectrum as a function of azimuthal mode order at (a) f = 400 Hz and (b) 2000 Hz. The four bars at each m indicates the eigenvalues of the first four POD modes n = 1, 2, 3 and 4.

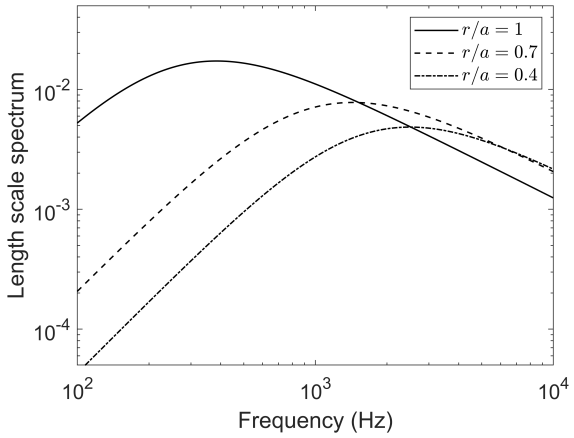

Fig. 9 Length-scale spectrum at various radial locations.

Figure 11 indicates that the lowest order modes are mostly responsible for reconstructing the large-scale coherent structure near the tip ($r/a = 1$), while higher order modes tend to be more spread across the radius to synthesise small scale structures away from the tip.

The reconstruction of the cross-spectral matrix based on different number of POD modes, N = 10, 40 and 70, at 400, 2000 and 4000 Hz are shown in Fig. 12. The actual cross-spectral matrices constructed using Eq. 30−32 are also presented for comparison. The first 10 modes are seen to capture the main feature at 400 Hz, i.e. the large-scale coherent structure near the tip, but are less satisfactory at 2000 and 4000 Hz. The reconstruction is much improved by increasing the number of modes from 20 to 40. When 70 modes are used, even the small scale details near the hub can be well captured.

The reconstructed velocity power spectral density (PSD) and cross-spectral density (CSD) based on 10, 40 and 70 POD modes are compared with the actual spectra in Fig. 13 to assess the reconstruction effectiveness over the whole

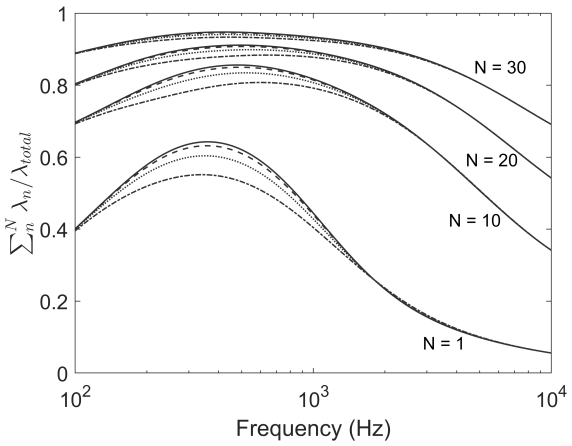

Fig. 10 Ratio of the truncated modal energy to the total energy as a function of frequency. *N* indicates the number of POD modes used to obtain the truncated energy. (——) $m = 0$, (- - -) $m = 20$, (·····) $m = 40$, (-·-·) $m = 60$.

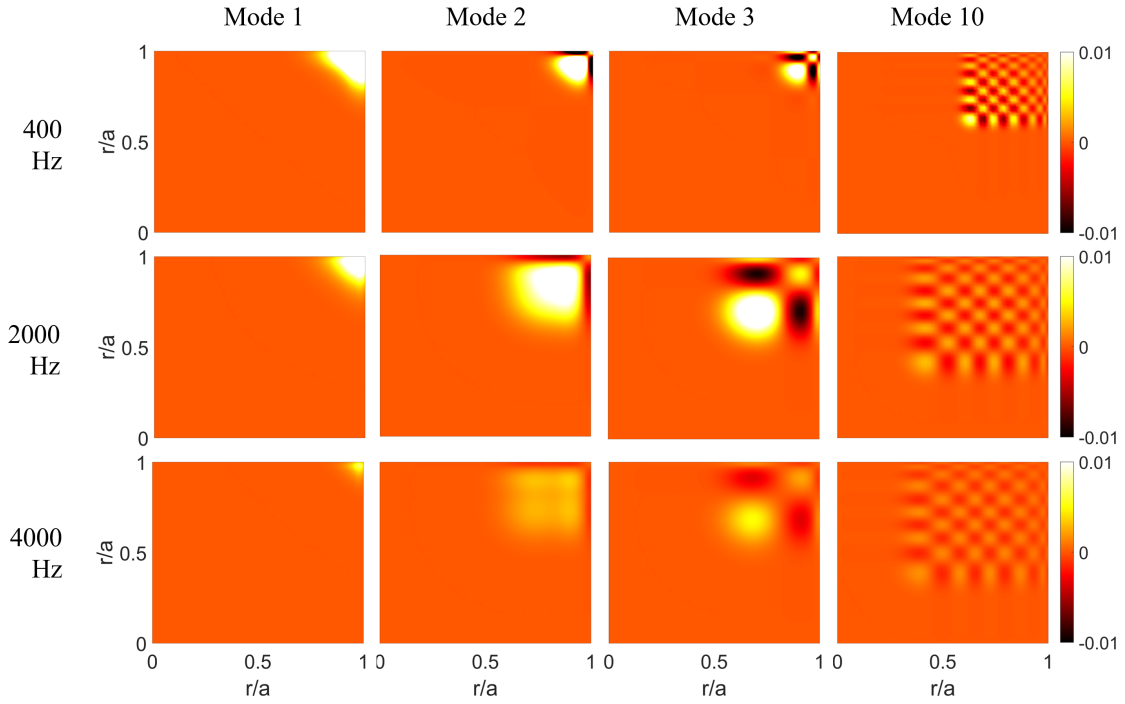

Fig. 11 Real part of cross-spectral matrix of POD mode 1, 2, 3 and 10 at $m = 0$ for different frequencies 400, 2000 and 4000 Hz.

frequency range. The results are presented at different radial locations. It is seen that the spectrum can be well recovered by using only the first 10 modes at locations near the tip (Fig. 13(a, d)) due to the presence of a large-scale coherent structure. For the locations closer to the hub (Fig. 13(b, c, e, f)), where smaller scale structures are dominant, many more modes are needed for a good reconstruction over most of the frequency range.

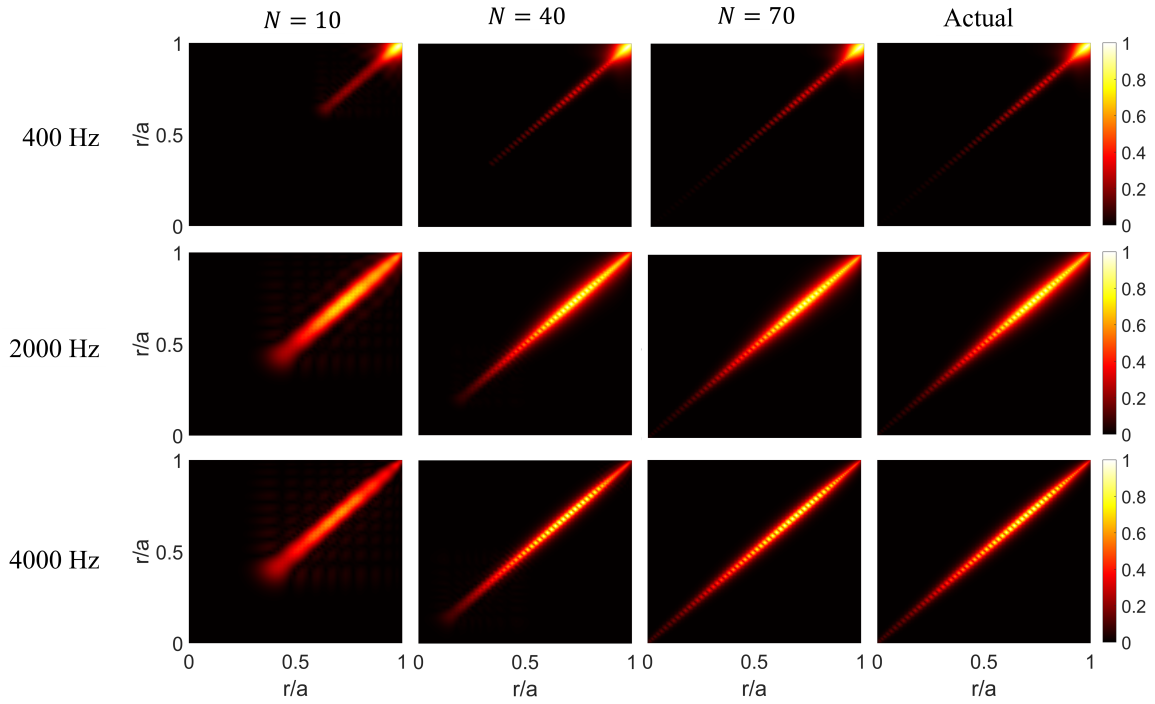

Fig. 12 Cross-spectral matrix reconstruction at m = 0 and different frequencies 400, 2000 and 4000 Hz based on different number of POD modes, N = 10, 40 and 70.

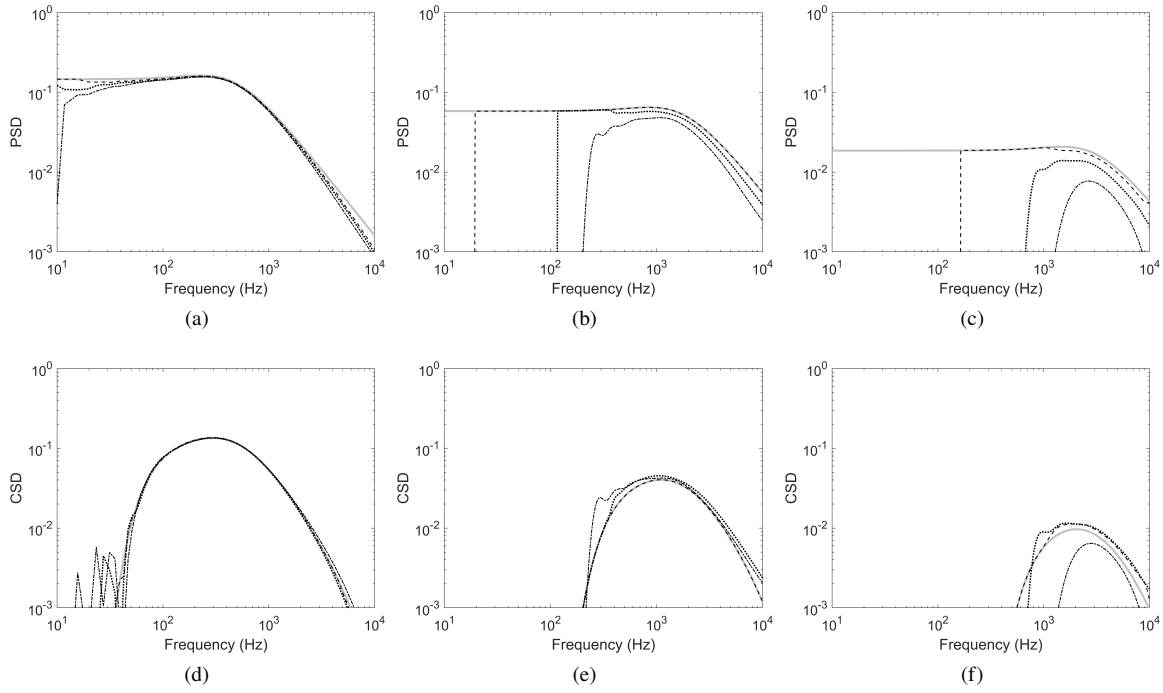

Fig. 13 Spectral POD reconstruction of PSD at (a) r/a = 1, (b) r/a = 0.7 and (c) r/a = 0.4, and CSD between (d) r/a = 1 and 0.98, (e) r/a = 0.7 and 0.68 and (f) r/a = 0.4 and 0.38. (-·-·) N = 10, (·····) N = 40, (- - -) N = 70, (——) Actual.

2. Fourier modes

In this section Fourier modes are used to reconstruct the radial cross-spectrum $C_m(r, r', \omega)$ through Eq. 11 by multiplying with the mode amplitude matrix $\hat{C}_m$ estimated from Eq. 20. A typical Fourier mode shape for the 10$^{\text{th}}$ radial mode is shown in Fig. 14. The POD mode shape at the same mode order is also shown for comparison. Note that the two modes have been normalised such that the integral over the area of the cross-section of the duct is unity,

$$A_{mn}^2 \int_0^{2\pi} \int_{r_h}^{r_t} \phi_{mn}(r, \omega) \phi_{mn}^*(r, \omega) r dr d\theta = 1, \tag{34}$$

where A_{mn} is the normalisation factor, which needs to be applied to the mode amplitude to normalise to unity the energy content within the corresponding mode.

Compared with the Fourier mode, which is evenly distributed along the radius, the POD mode is found to be more concentrated near the tip. In addition, the Fourier mode is independent of frequency, while the POD mode tends to spread towards the hub with increasing frequency as shown in Fig. 11.

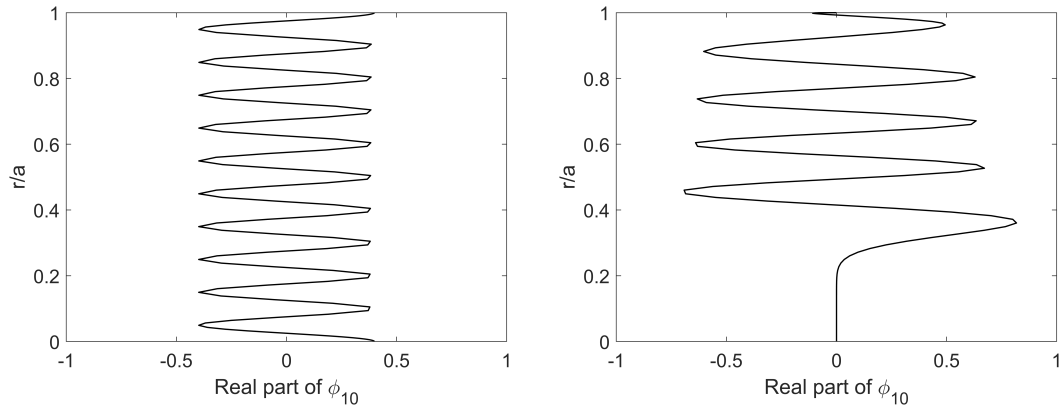

Fig. 14 (a) Fourier and (b) POD mode shape for n = 10 at 2000 Hz.

The reconstructed cross-spectral matrices obtained using the Fourier modes are compared with the actual result in Fig. 15 at $m = 0$ and 2000 Hz. The reconstructed results are based on $N = 11$, 41 and 71 modes with n from $-\frac{N-1}{2}$ to $\frac{N-1}{2}$ due to the symmetry of the Fourier decomposition. Compared with the POD-based reconstruction (see Fig. 12), the Fourier one shows more significant reconstruction errors when only 11 modes are used, especially for 400 Hz. Better agreement with the actual matrix is obtained by increasing the number of Fourier modes N from 11 to 41. However, further increasing N to 71 or more, the reconstructed matrices are found to be significantly contaminated by errors arising from the aliasing effects, while the POD method always behaves well. This observation suggests that the POD modes are more efficient and effective for the cross-spectral matrix reconstruction when the flow exhibits strong inhomogeneity.

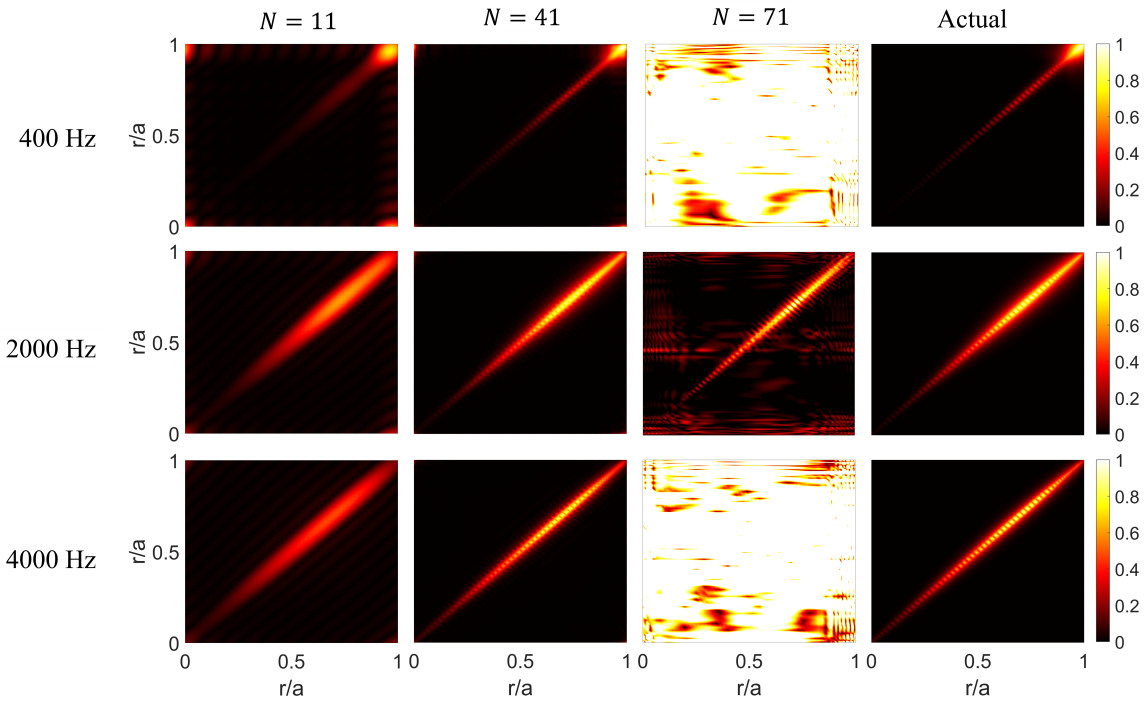

Fig. 15 Cross-spectral matrix reconstruction at m = 0 and different frequencies 400, 2000 and 4000 Hz based on different number of Fourier modes, N = 11, 41 and 71.

B. Time domain

We now investigate the use of POD modes for computing time domain velocity signals with the desired target cross-spectral velocity matrix. The turbulence velocity signals are then synthesised by filtering white noise signals in space and time using Eq. 29. The white noise signals are generated from a normal distribution with zero mean and and unit variance. The statistic convergence has been confirmed by comparing the spectra obtained from different number of samples for the white noise signal, 16k, 160k and 1600k, which showed little differences between 160k and 1600k. For simplicity, we only consider 1D turbulence synthesis in the radial direction and the subscript m is omitted. In this section, the reconstruction accuracy of the one- and two-point statistics is assessed. Comparisons are carried out between the actual spectra with those synthesised using time domain signals.

The synthesised auto and cross-correlation coefficients are compared with the actual results in Fig. 16. The coefficients are presented as a function of the time delay normalised by τ_c which is the radially averaged time scale. When the Taylor hypothesis is applied τ_c is simply obtained as,

$$\tau_c = \frac{\overline{\Lambda}}{\overline{U_c}}, \tag{35}$$

where the overline indicates radial averaging and the mean axial velocity U_x is regarded as the convection velocity $U_c = U_x$. The values of Λ and U_x were estimated from the RANS solution as a function radius, as shown in Section

IV.A.

Fig. 16(a) shows the autocorrelation coefficient, which is defined as,

$$\rho(r, r, \tau) = \frac{R(r, r, \tau)}{R(r, r, \tau = 0)}, \tag{36}$$

where $R(r, r, \tau)$ is the autocorrelation function. The actual target autocorrelation function can be derived from the actual PSD $C(r, r, \omega)$,

$$R_{\text{actual}}(r, r, \tau) = \int_{-\infty}^{\infty} C(r, r, \omega) e^{j\omega\tau} d\omega. \tag{37}$$

Using the synthesised signal $u(r, t)$, the synthesised autocorrelation function is given by,

$$R_{\text{syn}}(r, r, \tau) = E\left[u(r, t)u(r, t + \tau)\right]. \tag{38}$$

The cross-correlation coefficient shown in Fig. 16(b) is defined as,

$$\rho(r, r', \tau) = \frac{R(r, r', \tau)}{\sqrt{R(r, r, \tau = 0)R(r', r', \tau = 0)}}, \tag{39}$$

and the actual and synthesised cross-correlations are

$$R_{\text{actual}}(r, r', \tau) = \int_{-\infty}^{\infty} C(r, r', \omega) e^{i\omega\tau} d\omega, \tag{40}$$

$$R_{\text{syn}}(r, r', \tau) = E\left[u(r, t)u(r', t + \tau)\right]. \tag{41}$$

In Fig. 16, the autocorrelation functions are plotted for $r/a = 0.2$, 0.4, 0.6, 0.8 and 1, and the cross-correlations are between these points and their adjacent points with a separation distance of $\Delta r/a = 0.02$. Both the synthesised auto and cross correlation functions are in excellent agreement with the actual correlation functions although slight deviations are observed when the coefficients decrease to low values. Figure. 16 also shows that the flow is inhomogeneous in the radial direction. For homogeneous flows, the averaged correlation curves are expected to be identical along the radius. However, both the auto and cross correlations in Fig. 16 are seen to be dependent on the locations as they decrease quicker towards the hub, clearly indicating significant levels of inhomogeneity.

Taking the Fourier transform of the synthesised auto (Eq. 38) and cross (Eq. 41) correlations with respect to time gives the synthesised PSD and CSD, respectively. Comparison of the synthesised and actual cross-spectral matrix at three representative frequencies 400, 2000 and 4000 Hz are shown in Fig. 17. The synthesised spectra were estimated based on Welch's method using a Hanning window with segmental averaging applied over 100 segments (50% overlapped) of a sample length 10s, giving a frequency resolution of 10 Hz. The synthesised spectral matrices are

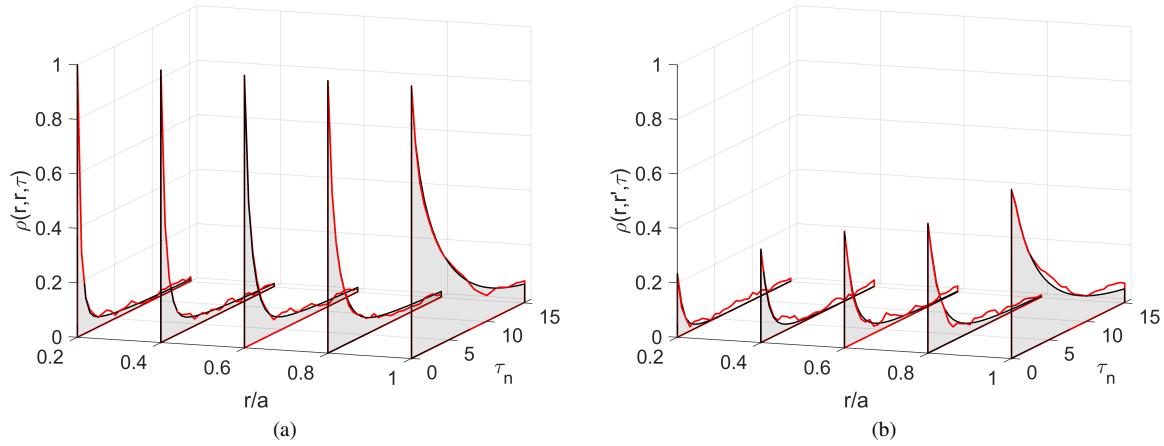

Fig. 16 Autocorrelation (a) and cross-correlation (b) coefficient as a function of normalized time lag $\tau_n = \tau/\tau_c$: (——) actual, (——) synthesised. The two points used for calculating cross-correlation have a separation distance $\Delta r/a = 0.02$.

seen to closely agree with the actual results despite the presence of small level of random noise, but whose amplitude is 10 times smaller than that along the diagonal $r = r'$ which can be reduced further by taking more averages in the spectral estimate. Further comparison for the spectrum over the whole frequency range is shown in Fig. 18. It is seen that the desired PSD and CSD spectra can be well reproduced by the synthesised signals for both locations.

VI. Application to fan/OGV interaction broadband noise

The proposed frequency-domain synthetic turbulence method is now coupled to a 3D frequency-domain LNS solver to predict the broadband noise due to the rotor-stator interaction for a realistic scale-model fan/OGV rig.

A. Computational setup and post-processing

The LNS solver used in the present study is the Rolls-Royce *plc* code, HYDRA, in which the linearised equations are solved using efficient second-order edge-based discretisation on unstructured hybrid grids [55, 56]. A 5-step Runge-Kutta algorithm, with an element collapsing multi-grid accelerator algorithm is used iteratively to converge to a steady state solution. The investigated case is ACAT1 fan at approach condition for which the noise measurement data are available in [7, 54, 57].

The acoustic calculations are performed on the OGV domain (see Fig.1). Considering the rotational periodicity of the flow, the domain can be reduced to a single vane passage with periodic boundary conditions applied in the circumferential direction. The periodic angle of the flow passage is determined by the inter-blade phase angle, i.e. $2\pi m/V$ where $V = 44$ is the OGV number in the present study. The vortical modal solutions obtained through the POD method as shown in Section II.A.1 are injected as input into the domain through the inlet boundary. It must be ensured that the injected modes are divergence-free to avoid the generation of spurious acoustic waves. The divergence-free

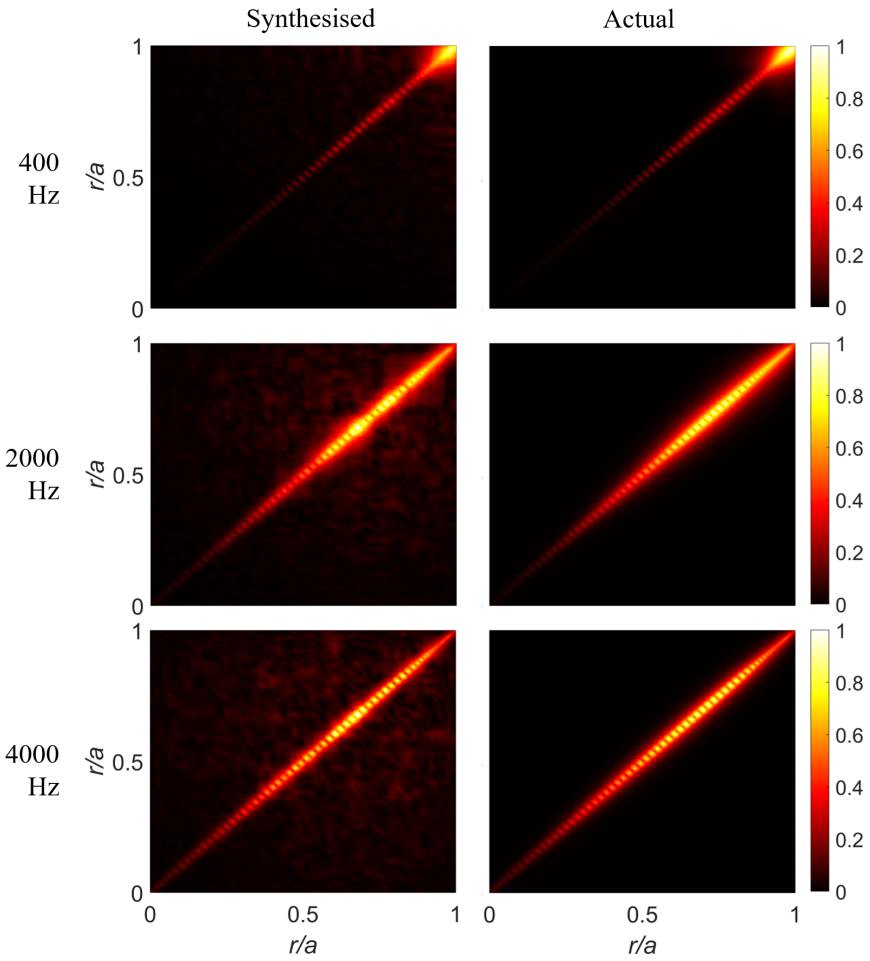

Fig. 17 Comparison of the synthesised and actual cross-spectral matrix at different frequencies 400, 2000 and 4000 Hz.

constraint can be easily imposed in the frequency domain by taking the inner product of the wavenumber and amplitude vectors to be zero, as shown in in Appendix A. Non-reflecting boundary conditions based on an eigenmode analysis of the unsteady flow field are applied at the inlet and outlet boundaries in order to minimize spurious reflections from the boundaries [58, 59]. Both the upstream and downstream mesh were expanded to achieve a pseudo-sponge layer to limit artificial reflection at the inlet and outlet boundaries.

The calculated unsteady solutions are post-processed to identify upstream and downstream acoustic waves using a wave-splitting technique [60] based on an eigenmode analysis. The eigen-solutions of the linearised equations involve three types of modes: acoustic, vortical and entropy modes. For uniform flows, the different types of modes are uncoupled. The acoustic modes are identified as those having significant pressure perturbations.

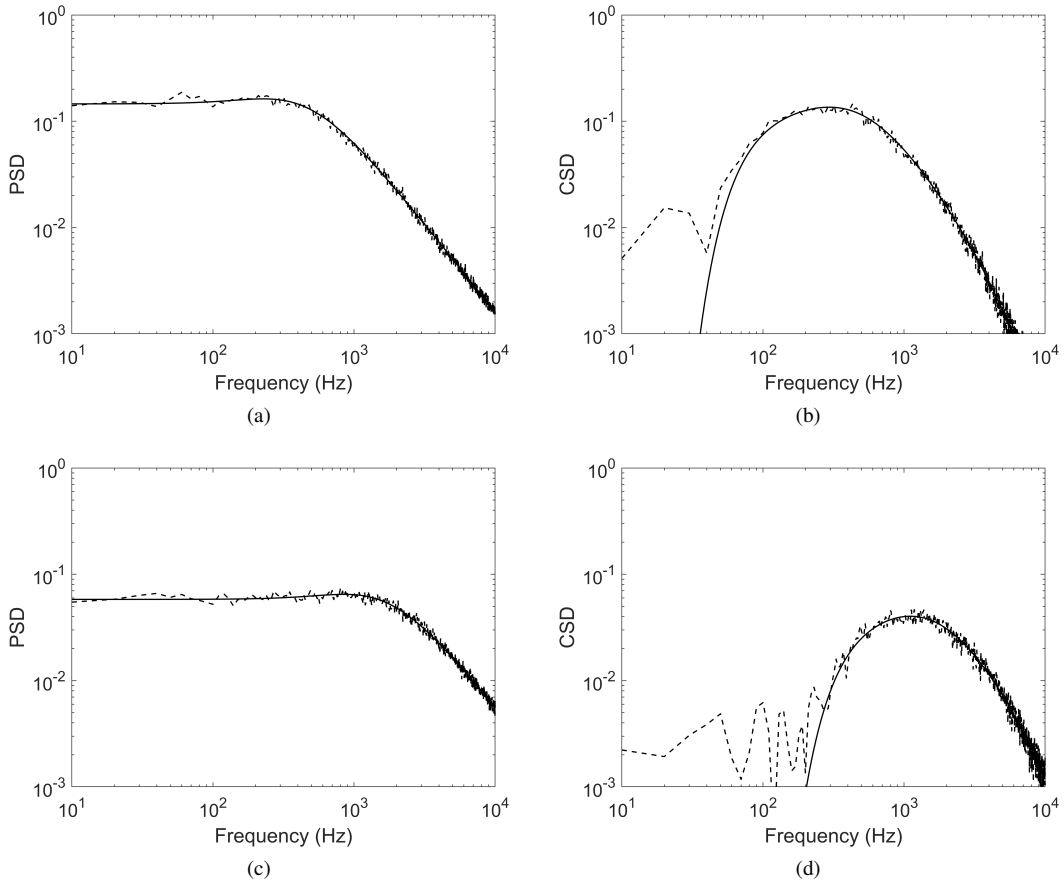

Fig. 18 Comparison of (- - -) the synthesised and (——) actual PSD at (a) r/a = 1 and (c) r/a = 0.7 and CSD between (a) r/a = 1 and 0.98 and (b) r/a = 0.7 and 0.68.

B. Radiated sound power

We now derive an expression for the radiated sound power generated by the impingement of the injected vortical disturbances onto the OGVs. Introducing a single vortical mode of order (m, n) with amplitude $\hat{u}_{mn}(\omega)$ into the computational domain produces a number of acoustic modal solutions [17, 60] i.e.,

$$p_{mn}(x, r, \theta, \omega) = \hat{u}_{mn}(\omega) \sum_{\mu\nu} \hat{p}_{mn,\mu\nu}(\omega)\psi_{mn,\mu\nu}(r)e^{i\mu\theta}e^{ik_{\mu\nu}x}. \tag{42}$$

where $p_{mn}(x, r, \theta, \omega)$ is the pressure field due to the incident vortical mode (m, n), $\psi_{mn,\mu\nu}(r)$ is the acoustic modal function (eigen-solution of the linearised equations) of order (μ, ν) associated with the incident vortical mode (m, n) and $\hat{p}_{mn,\mu\nu}(\omega)$ is the corresponding modal pressure amplitude.

The acoustic pressure $p_m(x, r, \theta, \omega)$ due to all vortical modes n simultaneously associated with a single value of m is therefore,

$$p_m(x,r,\theta,\omega) = \sum_n \hat{u}_{mn}(\omega) \sum_{\mu\nu} \hat{p}_{mn,\mu\nu}(\omega)\psi_{mn,\mu\nu}(r)e^{i\mu\theta}e^{ik_{\mu\nu}x}, \tag{43}$$

while the axial acoustic particle velocity associated with the vortical mode m is,

$$u_m(x,r,\theta,\omega) = \sum_n \hat{u}_{mn}(\omega) \sum_{\mu\nu} \hat{u}_{mn,\mu\nu}(\omega)\psi_{mn,\mu\nu}(r)e^{i\mu\theta}e^{ik_{\mu\nu}x}, \tag{44}$$

where $\hat{u}_{mn,\mu\nu}(\omega)$ is the particle velocity amplitude of the acoustic mode (μ,ν) due to the incident vortical mode (m,n).

At a single frequency the sound intensity due to all incident vortical modes associated with m is given by (assuming no swirl)

$$I_m^{\pm}(x,r,\theta,\omega) = \frac{1}{2}\mathrm{Re}\left\{ p_m u_m^{\pm *} + \rho_0 U_x u_m^{\pm} u_m^{\pm *} + \frac{U_x p_m p_m^*}{\rho_0 c_0^2} + \frac{U_x^2}{c_0^2} p_m^* u_m^{\pm} \right\}, \tag{45}$$

where ρ_0 is the mean density, c_0 is the speed of sound, and the subscript $\pm$ indicates upstream propagating (+) and downstream propagating (−) acoustic waves.

Substituting Eq. 43 and 44 for p_m and u_m, and taking the average of $\hat{u}_{mn}\hat{u}_{mn}^*$, the first term on the right hand side of Eq. 45 is written as,

$$\frac{1}{2}\mathrm{Re}\left\{ \sum_n \sum_{n'} E\left[\hat{u}_{mn}(\omega)\hat{u}_{mn'}^*(\omega)\right] \sum_{\mu\nu}\sum_{\mu'\nu'} \hat{p}_{mn,\mu\nu}(\omega)\hat{u}_{mn',\mu'\nu'}^{\pm *}(\omega)\psi_{mn,\mu\nu}(r)\psi_{mn',\mu'\nu'}^*(r)e^{i(\mu-\mu')\theta}e^{i(k_{\mu\nu}-k_{\mu'\nu'})x} \right\}, \tag{46}$$

where $E\left[\hat{u}_{mn}(\omega)\hat{u}_{mn'}^*(\omega)\right]$ represents the average modal energy of vortical modes for which the estimation procedure associated with the choice of modal functions is described in Section II. When vortical modes are represented by the POD modes it is shown in Eq. 16 that the amplitudes of different modes ($n \neq n'$) are uncorrelated, and Eq. 46 becomes

$$\frac{1}{2}\mathrm{Re}\left\{ \sum_n \lambda_{mn}(\omega) \sum_{\mu\nu}\sum_{\mu'\nu'} \hat{p}_{mn,\mu\nu}(\omega)\hat{u}_{mn,\mu'\nu'}^{\pm *}(\omega)\psi_{mn,\mu\nu}(r)\psi_{mn,\mu'\nu'}^*(r)e^{i(\mu-\mu')\theta}e^{i(k_{\mu\nu}-k_{\mu'\nu'})x} \right\}. \tag{47}$$

For a hard-walled duct the sound power W_m is obtained by integrating the axial acoustic intensity over the duct cross section,

$$W_m^{\pm} = \int_{r_h}^{r_t}\int_0^{2\pi} I_m^{\pm}(x,r,\theta,\omega) r dr d\theta. \tag{48}$$

The acoustic modes are assumed to be normalised and orthogonal, such that,

$$\int_{r_h}^{r_t} \psi_{\mu\nu}(r)\psi_{\mu'\nu'}(r)rdr \int_0^{2\pi} e^{i(\mu-\mu')\theta} d\theta e^{i(k_{\mu\nu}-k_{\mu'\nu'})x} = 2\pi\delta_{\mu\mu'}\delta_{\nu\nu'}\delta_{k_{\mu\nu}k_{\mu'\nu'}}, \tag{49}$$

Note that for a non-uniform swirling mean flow, the eigenfunctions $\psi_{\mu\nu}(r)$ are no longer orthogonal. In that case, interference occurs between different radial modes ($\nu \neq \nu'$), giving rise to non-zero value of the exponential term in Eq. 47 and the sound power varies with x [60, 61]. Nevertheless, in this study we focus on the noise downstream of the OGV where the flow field is relatively uniform and the assumption of orthogonality remains valid [60].

Substituting Eq. 45 into Eq. 48 and using Eq. 49, we have

$$W_m^{\pm}(\omega) = \pi \mathrm{Re}\Bigg\{ \sum_n \lambda_{mn}(\omega) \sum_{\mu\nu} \hat{p}_{mn,\mu\nu}(\omega)\hat{u}^{\pm *}_{mn,\mu\nu}(\omega) + \rho_0 U_x \hat{u}^{\pm}_{mn,\mu\nu}(\omega)\hat{u}^{\pm *}_{mn,\mu\nu}(\omega) + \frac{U_x}{\rho_0 c_0^2}\hat{p}_{mn,\mu\nu}(\omega)\hat{p}^{*}_{mn,\mu\nu}(\omega) + \frac{U_x^2}{c_0^2}\hat{p}^{*}_{mn,\mu\nu}(\omega)\hat{u}^{\pm}_{mn,\mu\nu}(\omega) \Bigg\}. \tag{50}$$

Note that in this prediction a single average value of U_x is used rather than the radial profile.

The total sound power at a single frequency $W^{\pm}(\omega)$ can therefore be simply obtained as an incoherent sum of the sound power per mode $W_{mn,\mu\nu}$,

$$W^{\pm}(\omega) = \sum_{mn} \lambda_{mn}(\omega) \sum_{\mu\nu} W^{\pm}_{mn,\mu\nu}(\omega). \tag{51}$$

Note that the above expression only applies when the turbulent field is expressed in terms of the POD modes. If using the Fourier modes, the total sound power can not be simply obtained as the incoherent sum of individual modal powers, as now the cross-terms ($n \neq n'$) of the vortical modal amplitude matrix (Eq. 20) are non-zero and the contributions from those cross-terms have to be taken into account.

C. Mesh sensitivity study

A mesh sensitivity study is conducted for $n = 10$ at $m = 40$ and 2BPF (corresponding to 2447 Hz) to ensure a sufficient grid solution to resolve the shortest wavelengths of the incident vortical modes or radiated acoustic cut-on modes. Table 3 provides a summary of the grid resolutions and computation time used for each grid case, where N_r, N_θ and N_x indicate the number of grid points used in the radial, circumferential and axial directions respectively and the total grid numbers for the coarse, medium and fine cases are 4, 7 and 12 millions respectively. Note that the computational time shown in Table. 3 is for a single input mode at a single frequency. A close-up view of the mesh with medium resolution is shown in Fig. 19.

The sensitivity of noise results to the grid refinement is assessed in Fig. 20 which shows the sound power levels (PWLs) of the upstream and downstream propagating wave components at different axial locations. The OGV is located

Table 3 Grid parameters and computational time.

Case	N_r	N_θ	Upstream N_x	Downstream N_x	Cells	Computational time
Coarse	86	80	155	185	4M	16 processors 12 hours
Medium	107	104	155	258	7M	64 processors 7 hours
Fine	136	140	178	360	12M	224 processors 8 hours

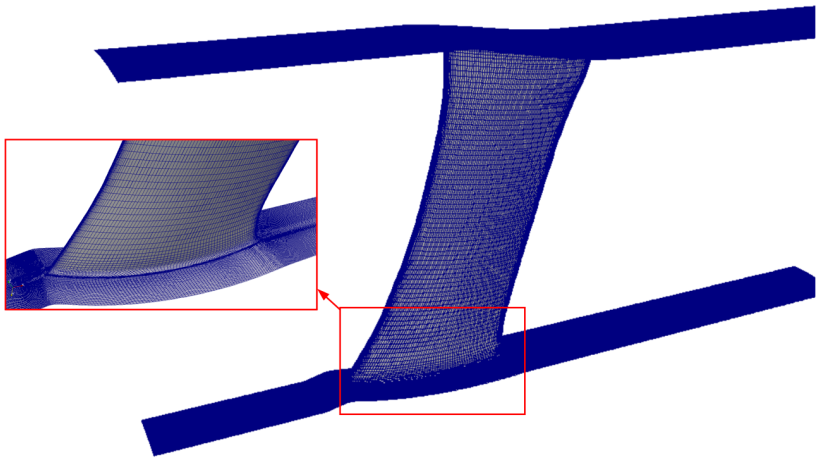

Fig. 19 Grid configuration for acoustic computation.

between $x = -2.59$ m and -2.54 m with $x < -2.59$ m indicating the upstream of OGV and $x > -2.53$ m the downstream. The scattered azimuthal acoustic mode orders due to the turbulence-cascade interaction can be calculated using the Tyler-Sofrin expression, $m + kV$, where k in this expression is the scattering index. Within each value of $m + kV$, there are a number of radial acoustic modes generated which can be identified as cut-on or cut-off depending on whether the imaginary parts of the mode axial wavenumbers (corresponding to the eigenvalues of the linearised equations) equal to zero or not. Different scattering indices at $k = -2, -1, 0, 1$ corresponding to $m + kV = -48, -4, 40$ and 84 have been examined, only $m + kV = -4$ is found to have radial cut-on acoustic modes. The PWLs shown in Fig. 20 are for $m + kV = -4$ where there were 6 radial cut-on acoustic modes identified with 3 propagating modes downstream and 3 upstream propagating modes.

Downstream of the OGV, the PWL of the downstream propagating modes are found to be about 20 dB higher than those of the upstream modes, thereby demonstrating the effectiveness of the non-reflecting boundary condition at the outlet boundary. The non-reflecting boundary condition also works well at the inlet boundary although the mean flow upstream of the OGV is non-uniform with swirl which might introduce difficulties for the wave-splitting at the inlet boundary. The much lower level of the downstream propagating wave at upstream of the OGV also implies that the divergence-free condition is effectively applied. In addition, at $m + kV = -4$ the PWLs of the cut-on modes remain constant across different axial locations which is as expected, since the sound power expression shown in Eq. 50 is a

function of ω only. The constant PWLs at upstream of the OGV, where swirling flow is present, also confirms that the contributions of the interference terms ($\nu \neq \nu'$ in Eq. 47) arising from the swirling effect to the total radiated sound power are negligible for the case under consideration. Figure 20 shows that refining the grid has negligible effect on the PWLs of the cut-on modes, suggesting that even the coarse grid resolution used in this study is sufficient for resolving the acoustic cut-on modes. This may be due to the fact that these cut-on modes are of low azimuthal and radial mode order.

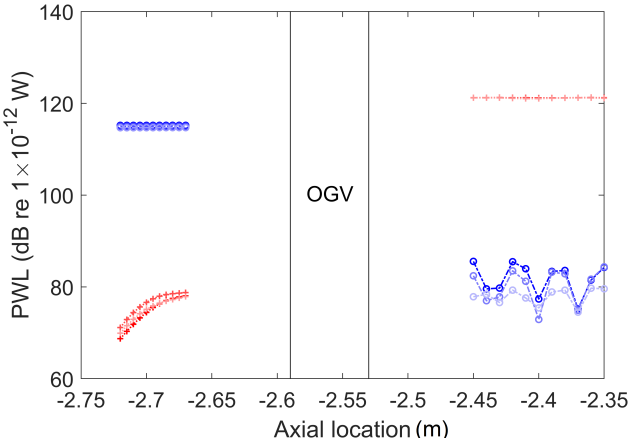

Fig. 20 Upstream -o and downstream –+ propagating waves at upstream and downstream of the OGV obtained using the POD mode input. The colour saturation from light to dark represents the mesh from coarse to fine.

D. Noise results

The real parts of the predicted axial velocity and pressure perturbations are plotted in Fig. 21 at the inlet and along a $x - \theta$ plane at the mid-radius over a full annular. The velocity perturbations at the inlet are seen to be concentrated close to the tip and no variation is observed at the hub, which are consistent with the POD mode shape shown in Fig. 14(b). The dominant acoustic cut-on mode corresponding to the interaction mode order $m + kV = -4$ is clearly identified in the pressure perturbation plot shown in Fig. 21(b) and a dipole source response is seen at the leading edge of the OGV.

It has been shown in Fig. 12 and 13 that to achieve a good reconstruction accuracy in the radial direction, at least 40 radial modes are required at 2000 Hz and even more at 4000 Hz. In the azimuthal direction, the eigenvalues were found to decrease slowly over m (Fig. 8), suggesting that many more modes may be needed for this direction. It is not feasible to perform acoustic computation for all these radial and azimuthal modes due to the expensive computational cost, so we need to determine how many radial and azimuthal modes are sufficient to provide a converged acoustic solution, which is illustrated in Fig. 22. Fig. 22(a) and (b) show the variations of the PWL with the incident radial and azimuthal modes n and m respectively. Here the PWL indicates the total sound power due to the contributions of all cut-on acoustic modes for a single incident vortical mode (m, n), represented by $\lambda_{mn} \sum_{\mu\nu} W^{\pm}_{mn,\mu\nu}(\omega)$ in Eq. 51. Fig. 22(c) and (d) show the cumulative PWLs which are obtained by taking the incoherent sum over $n = 1$ to N for radial modes and over $m = 2$ to M for azimuthal modes. Results in Fig. 22(a,c) correspond to a single azimuthal mode

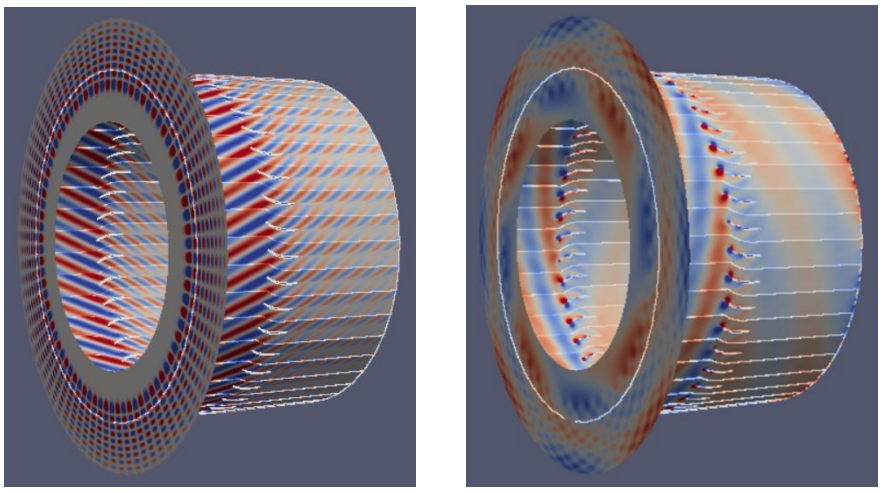

(a) (b)

Fig. 21 Real part of the axial velocity (a) and pressure (b) perturbations obtained using the POD mode input at $n = 10, m = 40$ and 2BPF

$m = 40$ at 2BPF. From Fig. 22(a), it is seen that above $n = 4$, the PWL decrease considerably with higher incident radial mode orders for both the upstream and downstream propagating waves. This is consistent with the findings by Atassi et al. [17] that higher order vortical modes are less efficient in scattering into the propagating low order acoustic modes. The cumulative PWLs (Fig. 22(b)) converge approximately at $n = 8$, with recognizing 1 dB difference with the level obtained based on 20 modes. The convergence with n was also assessed for other m, which showed similar trends.

Fig. 22(b) shows that the periodicity property in m observed for the 2D turbulence-cascade interaction noise case in [30] is also valid for this 3D case, where the interblade phase angle $2\pi m/V$ is important for determining radiation. For both the upstream and downstream propagating waves, the PWLs are seen periodic over incident azimuthal mode order m with a period $V = 44$. The difference in the cummulative PWL (Fig. 22(d)) between $M = 44$ and 82 is 1.2 dB.

The predicted PWL for downstream propagating waves at various frequencies are compared with the measured data from [7, 54, 57] in Fig. 23 where the LES results of Lewis et al. [11] are also included. According to the convergence of the cumulative PWLs obtained from Fig. 22, for each azimuthal vortical mode there are 8 radial vortical modes computed and there are 21 azimuthal vortical modes computed in total from $m = 2$ to 44 with $\Delta m = 2$ for each frequency. The sound power was measured in [7] from a modal breakdown of the noise in the bypass duct, from which the modal pressure amplitudes, and hence sound power contribution, of the dominant modes were determined. The main source of error arises from the presence of flow noise at the duct-wall microphones and aliasing effects of unresolved modes due to insufficient numbers of microphones. We would estimate the error / uncertainty of the spectral sound power estimate as being between 1 and 2 dB. Our prediction provides good agreement with the measurement at various frequencies. The maximum difference is 3.6 dB at 1BPF (corresponding to 1220 Hz) which is well within the range of the LES predictions [11] as well as the analytical predictions in [54] which were found to be generally 4-10 dB below

the measurement at frequencies below about 5000 Hz.

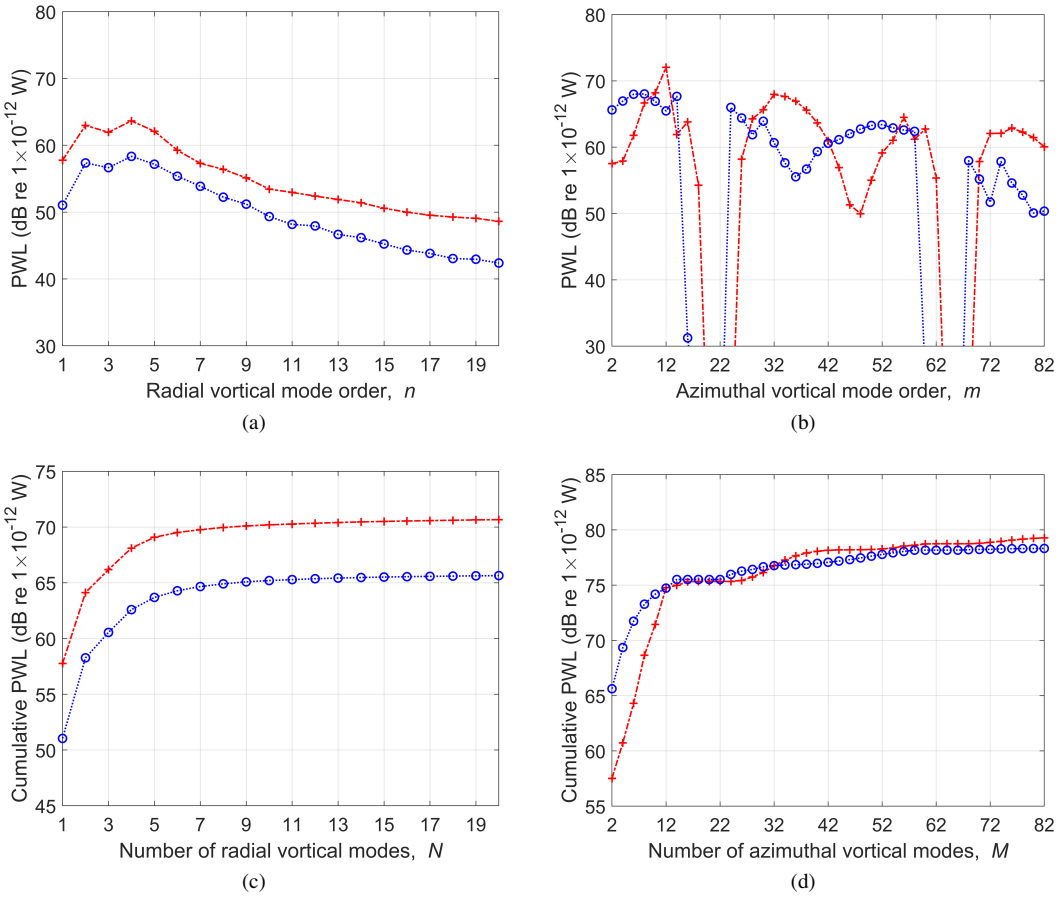

Fig. 22 (a) Variations of PWLs at $m = 40$ with incident radial vortical modes; (b) variations of PWLs at $n = 4$ with incident azimuthal vortical modes; (c) cumulative PWLs over different numbers of incident radial modes; (d) cumulative PWLs over different numbers of incident azimuthal modes. ·····o, upstream propagating wave; -·-·+, downstream propagating wave.

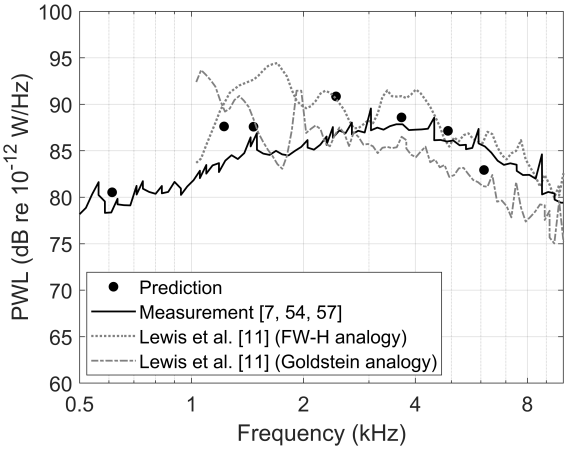

Fig. 23 Comparisons of the predicted PWLs at various frequencies with the measurements [7, 54, 57] and the LES results of Lewis et al. [11] based on FW-H and Goldstein's analogies.

E. Modal radiation efficiency

The radiation efficiency of a single mode, referred to as the modal radiation efficiency, is investigated in this section. The radiation efficiency is defined as the ratio of the radiated sound power W of a given structure to that produced by an ideal case of a piston of the same surface area vibrating with the same mean-square velocity and producing plane waves, which can be written as:

$$\eta = \frac{W}{\rho_0 c S E[\overline{v^2}]} \tag{52}$$

where S is the surface area and $E[\overline{v^2}]$ is the spatially-averaged mean-square vibration velocity normal to the surface. Both W and $E[\overline{v^2}]$ are functions of frequency. The denominator in Eq. 52 represents the sound power that would be radiated by the ideal case. The above expression is to assess the total sound power – the summation over all vibration modes. It is also possible to determine the radiation efficiency for each single mode. In this study, the vortical modes resembles the vibration modes and our aim is to assess how efficient each vortical mode is in radiating sound power. The modal radiation efficiency may therefore be expressed as:

$$\eta = \frac{W^{\pm}_{mn}(\omega)}{\rho_0 c S E[\overline{|u_{mn}(\omega)|^2}]} \tag{53}$$

where $W^{\pm}_{mn}(\omega)$ indicates the sound power radiated due to a single incident vortical mode (m, n), represented by $\lambda_{mn} \sum_{\mu\nu} W^{\pm}_{mn,\mu\nu}(\omega)$ in Eq. 51, $E[\overline{|u_{mn}(\omega)|^2}]$ is the spatially-averaged mean-square velocity of the vortical mode (m, n), which corresponds to $\lambda_{mn}(\omega)$ according to Eq. 16 and S is the area of the duct cross-section.

The modal radiation efficiency is plotted as a function of azimuthal vortical mode order in Fig. 24 for different radial modes $n = 1, 3, 5$ and 7 at various frequencies, 2BPF, 3BPF, 4BPF and 5BPF. The results are for the downstream propagating waves. It is seen that the radiation efficiency decreases significantly between $m = 20$ and 24 for 2BPF as no acoustic cut-on modes were identified. For 4BPF and 5BPF, all azimuthal orders show at least one cut-on mode, and the radiation is less efficient at 5BPF. The radiation efficiency is also found to vary with the incident radial order n, particularly at m close to the cut-off modes, suggesting that the radial variation of the incident vortical mode also has an effect on the scattered acoustic mode propagation. It is interesting to note that the first incident radial mode $n = 1$ is always less efficient than other radial orders at about $m > 26$ for different frequencies. The reason is not yet clear. The much lower radiation efficiency at $n = 1$ for all m at 5BPF may be explained by the fact that at this frequency, the radial variation of the first vortical mode only occurs in an extremely small region near the tip, similar to the pattern shown in Fig. 11 for 4000 Hz.

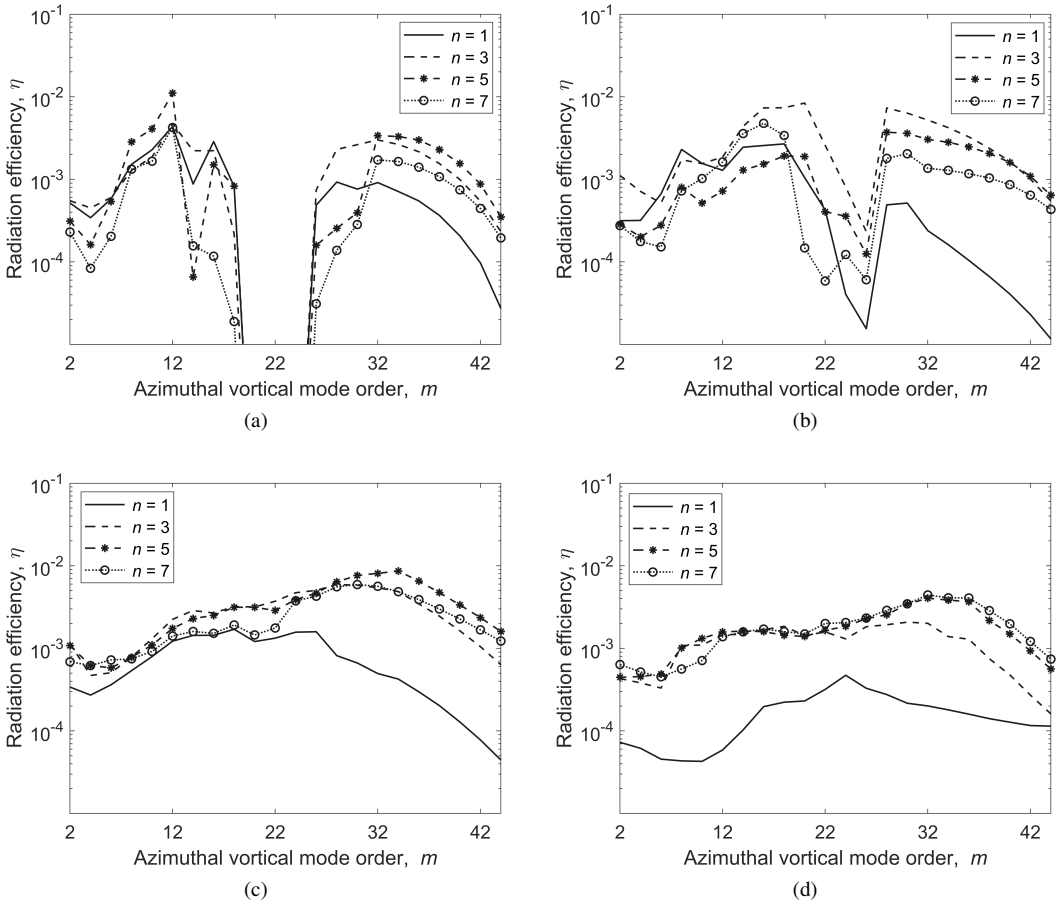

Fig. 24 Radiation efficiency as a function of incident azimuthal mode order for different radial mode order n at (a) 2BPF, (b) 3BPF, (c) 4BPF and (d) 5BPF.

VII. Critique of the POD method for fan broadband noise prediction

A novel feature of this study is the use of the POD-based synthetic turbulence method for fan broadband noise prediction. The advantages of this POD method are fourfold. First, the POD modes provide the most efficient and accurate representation of the cross-spectral matrix for inhomogeneous flows. The efficiency has been investigated in Fig. 10 which shows that only the leading 10 POD modes are able to capture nearly 80% of the total energy at frequencies around 400 Hz where a large-scale coherent structure is present. It is also shown in Section V.A that both the cross-spectral matrices at various frequencies (see Fig. 12) and the cross-spectra at various locations (see Fig. 13) can be accurately reconstructed using the POD modes, although the reconstruction efficiency reduces at high frequencies where the small-scale structures are dominant. Second, the dominant large-scale coherent structure near the tip can be well identified by the leading POD modes, as seen in Fig. 12 at 400 Hz. Furthermore, by making use of the property that the amplitudes of different POD modes are uncorrelated (see Eq. 16), the total sound power calculation can be simplified as an incoherent sum of the sound power per mode (Eq. 51). If using the Fourier modes or other types of

modes, such as the normal modes of LEE, there will be non-zero off diagonal entries in the modal amplitude matrix (Eq. 20), so the contributions due to the coupling of different modes to the total sound power have to be considered (since Eq. 46 cannot be simplified to Eq. 47). However, it should be mentioned that when the flow is homogeneous, the Fourier modes are equivalent to the POD modes and the total sound power calculation is exactly the same as in Eq. 51. Lastly, the POD method is expected to be more efficient than the Fourier method also in acoustic computation. This is because the POD is able to capture the dominant vortical modes with the largest amplitudes, thus a smaller number of input modes may be needed to get a converged acoustic solution than using the Fourier modes. This is particularly important for the frequency domain computation.

Nevertheless, this method has some limitations. The POD modes are found to be inefficient in spectral reconstruction at high frequencies where the small-scale structures are dominant. In addition, for homogeneous flows, the POD modes reduce to the Fourier modes and a large number of modes might be needed for the spectral reconstruction as well as the acoustic computation.

VIII. Conclusion

This paper proposed a synthetic turbulence method aiming to reproduce the desired velocity cross-spectrum over the OGV leading edge for the use in the fan/OGV interaction broadband noise prediction. The method was developed first in frequency domain based on a superposition of vortical modes with the appropriate amplitudes. Two different modal approaches, POD modes and Fourier modes, have been proposed and the POD method was investigated in detail in this paper.

Through the analysis in frequency domain, it was found that the spectral reconstruction efficiency of the POD modes is closely related to the existence of localised coherent structures. At the spectral peak frequency around 400 Hz where a large-scale coherent structure was observed near the tip, the first POD mode was found to contain more than 50% of the total kinetic energy and a good reconstruction was achieved by using the few leading modes. The dominance of the first mode becomes weak at high frequencies where small scales become dominant and much more modes are therefore needed for the reconstruction. It was also found that varying the azimuthal mode has only small effects on the energy recovery. The Fourier modes were also investigated and found to be less efficient than the POD modes in the spectral reconstruction as more significant reconstruction error was observed when only using the few leading modes. These findings clearly show that the POD method is the most efficient and accurate in the representation of inhomogeneous turbulence, especially when large-scale coherent structures are present.

The POD method was then extended to time domain through a white noise filtering process to allow for the potential application in generating synthetic turbulence in the time domain CAA solver, for example time domain Euler solver, LES or LBM. For the reconstruction in time domain, both the one- and two-point statistics were well reproduced using the synthesised velocity signals obtained from the POD modes. The synthesised PSD and CSD showed a good match

with the actual results in terms of both the spectral shape and levels.

The proposed frequency-domain POD synthetic turbulence method was validated by coupling to a frequency-domain LNS solver for the broadband noise prediction on ACAT1 fan at approach condition. By making use of the property that amplitudes of different POD modes are uncorrelated, the total sound power calculation has been simplified as an incoherent sum of the sound power per mode. Good agreement is obtained between the predicted sound power levels and the measured ones at various frequencies, with a maximum difference of 3.6 dB observed at 1BPF.

Appendix A. Imposing the divergence-free constraint in frequency domain

A schematic of rotor-OGV diagram with velocity triangles is shown in Fig. 25. The desired cross-spectral matrix C_m is for the upwash velocity fluctuation normal to the chord, which can be expressed in terms of the azimuthal and axial fluctuation components, u_θ and u_x respectively, as,

$$u_n = \frac{-u_x U_\theta + u_\theta U_x}{U_s}, \tag{54}$$

where u_n now refers to the normal component of velocity and where U_θ and U_x are the mean azimuthal and axial velocity components respectively, and $U_s = \sqrt{U_\theta^2 + U_x^2}$ is the mean velocity component along the streamlines, which are assumed to be fully aligned with the chord.

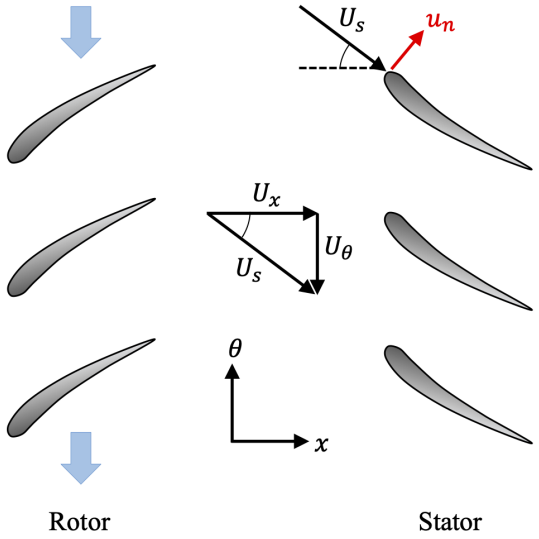

Fig. 25 Velocity diagram and upwash velocity fluctuation u_n (normal to the streamlines U_s).

The divergence-free constraint for incompressible flows can be imposed in the frequency domain by setting the inner product of the wavenumber and amplitude vectors to zero (i.e. they are orthogonal),

$$\nabla \cdot \mathbf{u} = \alpha u_x + \beta u_\theta = 0, \tag{55}$$

where α and β are the wavenumbers of the perturbation quantities in the axial and azimuthal directions respectively. For m^{th} azimuthal mode order, $\beta = m/r$. Using the dispersion relation derived in [62] for vortical waves, we obtain $\alpha = \frac{\omega}{U_x} - \frac{mU_\theta}{rU_x}$.

Following the work of Atassi et al. [17] the velocity components (u_x, u_r, u_θ) of the vortical modes can be deduced from the normal component u_n. Using Eq. 54 and 55,

$$u_x = -\frac{mu_n U_s}{\alpha r U_x + mU_\theta}, \tag{56}$$

$$u_\theta = -\frac{\alpha r u_n U_s}{\alpha r U_x + mU_\theta}. \tag{57}$$

Note that by way of an approximation, we have only imposed the divergence-free constraint in the $x - \theta$ plane since we understand that the u_r does not contribute to the noise. An assumption of $u_r = 0$ is usually made in the literature for fan broadband noise prediction, for example in [17]. A similar approximation was also made by Goldstein [63] in the analysis of loading noise.

Acknowledgments

This work was partly supported by Aerospace Technology Institute (ATI) funded programme ACAPELLA and EU 2020 funded TurboNoiseBB at the University of Southampton. The authors would like to thank Anecom and TurbonoiseBB for providing the data. The authors would also like to thank Rolls-Royce for technical support.

References

[1] Amiet, R. K., "Acoustic radiation from an airfoil in a turbulent stream," *Journal of Sound and Vibration*, Vol. 41, No. 4, 1975, pp. 407–420. URL https://doi.org/10.1016/S0022-460X(75)80105-2.

[2] Hanson, D., and Horan, K., "Turbulence/cascade interaction-Spectra of inflow, cascade response, and noise," *4th AIAA/CEAS Aeroacoustics Conference*, 1998, p. 2319. URL https://doi.org/10.2514/6.1998-2319.

[3] Glegg, S. A., "The response of a swept blade row to a three-dimensional gust," *Journal of sound and vibration*, Vol. 227, No. 1, 1999, pp. 29–64. URL https://doi.org/10.1006/jsvi.1999.2327.

[4] Cheong, C., Joseph, P., and Lee, S., "High frequency formulation for the acoustic power spectrum due to cascade-turbulence interaction," *The Journal of the Acoustical Society of America*, Vol. 119, No. 1, 2006, pp. 108–122. URL https://doi.org/10.1121/1.2139626.

[5] Posson, H., Moreau, S., and Roger, M., "On the use of a uniformly valid analytical cascade response function for fan broadband noise predictions," *Journal of Sound and Vibration*, Vol. 329, No. 18, 2010, pp. 3721–3743. URL https://doi.org/10.1016/j.jsv.2010.03.009.

[6] Ganz, U. W., Joppa, P. D., Patten, T. J., and Scharpf, D. F., "Boeing 18-inch fan rig broadband noise test," *NASA CR-208704*, 1998.

[7] Tapken, U., Behn, M., Spitalny, M., and Pardowitz, B., "Radial mode breakdown of the ACAT1 fan broadband noise generation in the bypass duct using a sparse sensor array," *25th AIAA/CEAS Aeroacoustics Conference*, 2019, p. 2525. URL https://doi.org/10.2514/6.2019-2525.

[8] Lewis, D., de Laborderie, J., Sanjosé, M., Moreau, S., Jacob, M. C., and Masson, V., "Parametric study on state-of-the-art analytical models for fan broadband interaction noise predictions," *Journal of Sound and Vibration*, Vol. 514, 2021, p. 116423. URL https://doi.org/10.1016/j.jsv.2021.116423.

[9] Shur, M., Strelets, M., Travin, A., Spalart, P., and Suzuki, T., "Unsteady simulations of a fan/outlet-guide-vane system: Aerodynamics and turbulence," *AIAA Journal*, Vol. 56, No. 6, 2018, pp. 2283–2297. URL https://doi.org/10.2514/1.J056645.

[10] Suzuki, T., Spalart, P. R., Shur, M. L., Strelets, M. K., and Travin, A. K., "Unsteady simulations of a fan/outlet-guide-vane system: broadband-noise computation," *AIAA Journal*, Vol. 57, No. 12, 2019, pp. 5168–5181. URL https://doi.org/10.2514/1.J058177.

[11] Lewis, D., Moreau, S., and Jacob, M. C., "Broadband noise predictions on the ACAT1 fan stage using large eddy simulations and analytical models," *AIAA aviation 2020 forum, Virtual event*, 2020, p. 2519. URL https://doi.org/10.2514/6.2020-2519.

[12] Arroyo, C. P., Leonard, T., Sanjose, M., Moreau, S., and Duchaine, F., "Large Eddy Simulation of a scale-model turbofan for fan noise source diagnostic," *Journal of Sound and Vibration*, Vol. 445, 2019, pp. 64–76. URL https://doi.org/10.1016/j.jsv.2019.01.005.

[13] Kholodov, P., and Moreau, S., "Identification of noise sources in a realistic turbofan rotor using Large Eddy Simulation," *Acoustics*, Vol. 2, Multidisciplinary Digital Publishing Institute, 2020, pp. 691–706. URL https://doi.org/10.3390/acoustics2030037.

[14] Casalino, D., Hazir, A., and Mann, A., "Turbofan broadband noise prediction using the lattice Boltzmann method," *AIAA Journal*, Vol. 56, No. 2, 2018, pp. 609–628. URL https://doi.org/10.2514/1.J055674.

[15] Gonzalez-Martino, I., and Casalino, D., "Fan tonal and broadband noise simulations at transonic operating conditions using lattice-Boltzmann methods," *2018 AIAA/CEAS aeroacoustics conference*, 2018, p. 3919. URL https://doi.org/10.2514/6.2018-3919.

[16] Golubev, V. V., and Atassi, H. M., "Unsteady swirling flows in annular cascades, part 1: evolution of incident disturbances," *AIAA Journal*, Vol. 38, No. 7, 2000, pp. 1142–1149. URL https://doi.org/10.2514/2.1107.

[17] Atassi, H., Ali, A., Atassi, O., and Vinogradov, I., "Scattering of incident disturbances by an annular cascade in a swirling flow," *Journal of Fluid Mechanics*, Vol. 499, 2004, p. 111. URL https://doi.org/10.1017/S0022112003007031.

[18] Paruchuri, C. C., Coupland, J., and Joseph, P., "Airfoil geometry effects on turbulence interaction noise in cascades," *22nd AIAA/CEAS Aeroacoustics Conference*, 2016, p. 2738. URL https://doi.org/10.2514/6.2016-2738.

[19] Dieste, M., and Gabard, G., "Random particle methods applied to broadband fan interaction noise," *Journal of Computational Physics*, Vol. 231, No. 24, 2012, pp. 8133–8151. URL https://doi.org/10.1016/j.jcp.2012.07.044.

[20] Wohlbrandt, A. M., Guérin, S., and Ewert, R., "Simultaneous computation of surface and volume sources for fan broadband noise with the Random-Particle-Mesh method," *19th AIAA/CEAS aeroacoustics conference*, 2013, p. 2119. URL https://doi.org/10.2514/6.2013-2119.

[21] Polacsek, C., Clair, V., Le Garrec, T., Reboul, G., and Jacob, M. C., "Numerical predictions of turbulence/cascade-interaction noise using computational aeroacoustics with a stochastic model," *AIAA Journal*, Vol. 53, No. 12, 2015, pp. 3551–3566. URL https://doi.org/10.2514/1.J053896.

[22] Cader, A., Polacsek, C., Le Garrec, T., Barrier, R., Benjamin, F., and Jacob, M. C., "Numerical prediction of rotor-stator interaction noise using 3D CAA with synthetic turbulence injection," *2018 AIAA/CEAS Aeroacoustics Conference*, 2018, p. 4190. URL https://doi.org/10.2514/6.2018-4190.

[23] Kissner, C., and Guérin, S., "Comparison of predicted fan broadband noise using a two-versus a three-dimensional synthetic turbulence method," *Journal of Sound and Vibration*, Vol. 508, 2021, p. 116221. URL https://doi.org/10.1016/j.jsv.2021.116221.

[24] Polacsek, C., Cader, A., Buszyk, M., Barrier, R., Gea-Aguilera, F., and Posson, H., "Aeroacoustic design and broadband noise predictions of a fan stage with serrated outlet guide vanes," *Physics of Fluids*, Vol. 32, No. 10, 2020, p. 107107. URL https://doi.org/10.1063/5.0020190.

[25] Glegg, S. A., and Devenport, W. J., "Proper orthogonal decomposition of turbulent flows for aeroacoustic and hydroacoustic applications," *Journal of Sound and Vibration*, Vol. 239, No. 4, 2001, pp. 767–784. URL https://doi.org/10.1006/jsvi.2000.3128.

[26] Kraichnan, R. H., "Diffusion by a random velocity field," *The Physics of Fluids*, Vol. 13, No. 1, 1970, pp. 22–31. URL https://doi.org/10.1063/1.1692799.

[27] Karweit, M., Blanc-Benon, P., Juvé, D., and Comte-Bellot, G., "Simulation of the propagation of an acoustic wave through a turbulent velocity field: A study of phase variance," *The Journal of the Acoustical Society of America*, Vol. 89, No. 1, 1991, pp. 52–62. URL https://doi.org/10.1121/1.400415.

[28] Bechara, W., Bailly, C., Lafon, P., and Candel, S. M., "Stochastic approach to noise modeling for free turbulent flows," *AIAA Journal*, Vol. 32, No. 3, 1994, pp. 455–463. URL https://doi.org/10.2514/3.12008.

[29] Bailly, C., and Juve, D., "A stochastic approach to compute subsonic noise using linearized Euler's equations," *5th AIAA/CEAS aeroacoustics conference and exhibit*, 1999, p. 1872. URL https://doi.org/10.2514/6.1999-1872.

[30] Paruchuri, C., Gill, J. R., Subramanian, N., Joseph, P., Vanderwel, C., Zhang, X., and Ganapathisubramani, B., "Aerofoil geometry effects on turbulence interaction noise," *21st AIAA/CEAS aeroacoustics conference*, 2015, p. 2830. URL https://doi.org/10.2514/6.2015-2830.

[31] Blázquez-Navarro, R., and Corral, R., "Prediction of fan acoustic blockage on fan/outlet guide vane broadband interaction noise using frequency domain linearised Navier–Stokes solvers," *Journal of Sound and Vibration*, Vol. 500, 2021, p. 116033. URL https://doi.org/10.1016/j.jsv.2021.116033.

[32] Grace, S., Gonzalez-Martino, I., and Casalino, D., "Analysis of fan-stage gap-flow data to inform simulation of fan broadband noise," *Philosophical Transactions of the Royal Society A*, Vol. 377, No. 2159, 2019, p. 20190080. URL https://doi.org/10.1098/rsta.2019.0080.

[33] Gea-Aguilera, F., Gill, J., and Zhang, X., "Synthetic turbulence methods for computational aeroacoustic simulations of leading edge noise," *Computers & Fluids*, Vol. 157, 2017, pp. 240–252. URL https://doi.org/10.1016/j.compfluid.2017.08.039.

[34] Ewert, R., "Broadband slat noise prediction based on CAA and stochastic sound sources from a fast random particle-mesh (RPM) method," *Computers & Fluids*, Vol. 37, No. 4, 2008, pp. 369–387. URL https://doi.org/10.1016/j.compfluid.2007.02.003.

[35] Kim, J. W., and Haeri, S., "An advanced synthetic eddy method for the computation of aerofoil–turbulence interaction noise," *Journal of Computational Physics*, Vol. 287, 2015, pp. 1–17. URL https://doi.org/10.1016/j.jcp.2015.01.039.

[36] Jarrin, N., Benhamadouche, S., Laurence, D., and Prosser, R., "A synthetic-eddy-method for generating inflow conditions for large-eddy simulations," *International Journal of Heat and Fluid Flow*, Vol. 27, No. 4, 2006, pp. 585–593. URL https://doi.org/10.1016/j.ijheatfluidflow.2006.02.006.

[37] Sescu, A., and Hixon, R., "Toward low-noise synthetic turbulent inflow conditions for aeroacoustic calculations," *International Journal for Numerical Methods in Fluids*, Vol. 73, No. 12, 2013, pp. 1001–1010. URL https://doi.org/10.1002/fld.3833.

[38] Klein, M., Sadiki, A., and Janicka, J., "A digital filter based generation of inflow data for spatially developing direct numerical or large eddy simulations," *Journal of Computational Physics*, Vol. 186, No. 2, 2003, pp. 652–665. URL https://doi.org/10.1016/S0021-9991(03)00090-1.

[39] Ewert, R., Dierke, J., Siebert, J., Neifeld, A., Appel, C., Siefert, M., and Kornow, O., "CAA broadband noise prediction for aeroacoustic design," *Journal of Sound and Vibration*, Vol. 330, No. 17, 2011, pp. 4139–4160. URL https://doi.org/10.1016/j.jsv.2011.04.014.

[40] Hainaut, T., Gabard, G., and Clair, V., "A caa study of turbulence distortion in broadband fan interaction noise," *22nd AIAA/CEAS Aeroacoustics Conference*, 2016, p. 2839. URL https://doi.org/10.2514/6.2016-2839.

[41] Wohlbrandt, A., Hu, N., Guerin, S., and Ewert, R., "Analytical reconstruction of isotropic turbulence spectra based on the Gaussian transform," *Computers & Fluids*, Vol. 132, 2016, pp. 46–50. URL https://doi.org/10.1016/j.compfluid.2016.03.023.

[42] Gea-Aguilera, F., Gill, J., and Zhang, X., "On the effects of fan wake modelling and vane design on cascade noise," *Journal of Sound and Vibration*, Vol. 459, 2019, p. 114859. URL https://doi.org/10.1016/j.jsv.2019.114859.

[43] Gea-Aguilera, F., Karve, R., Gill, J., Zhang, X., and Angland, D., "On the effects of anisotropic turbulence on leading edge noise," *Journal of Sound and Vibration*, Vol. 495, 2021, p. 115895. URL https://doi.org/10.1016/j.jsv.2020.115895.

[44] Perret, L., Delville, J., Manceau, R., and Bonnet, J.-P., "Turbulent inflow conditions for large-eddy simulation based on low-order empirical model," *Physics of Fluids*, Vol. 20, No. 7, 2008, p. 075107. URL https://doi.org/10.1063/1.2957019.

[45] Towne, A., Schmidt, O. T., and Colonius, T., "Spectral proper orthogonal decomposition and its relationship to dynamic mode decomposition and resolvent analysis," *Journal of Fluid Mechanics*, Vol. 847, 2017, pp. 821–867. URL https://doi.org/10.1017/jfm.2018.283.

[46] Blandeau, V., "Aerodynamic broadband noise from contra-rotating open rotors," Ph.D. thesis, University of Southampton, 2011.

[47] Lumley, J., "The structure of inhomogeneous turbulent flows," *Atmospheric Turbulence and Radio Wave Propagation*, 1967, pp. 166–176.

[48] Schmidt, O. T., and Colonius, T., "Guide to spectral proper orthogonal decomposition," *Aiaa journal*, Vol. 58, No. 3, 2020, pp. 1023–1033. URL https://doi.org/10.2514/1.J058809.

[49] Berkooz, G., Holmes, P., and Lumley, J. L., "The proper orthogonal decomposition in the analysis of turbulent flows," *Annual Review of Fluid Mechanics*, Vol. 25, No. 1, 1993, pp. 539–575. URL https://doi.org/10.1146/annurev.fl.25.010193.002543.

[50] Strang, G., *Introduction to Linear Algebra*, Wellesley-Cambridge Press, MA, USA, 2003.

[51] Menter, F. R., "Two-equation eddy-viscosity turbulence models for engineering applications," *AIAA Journal*, Vol. 32, No. 8, 1994, pp. 1598–1605. URL https://doi.org/10.2514/3.12149.

[52] Paruchuri, C., Joseph, P., Mao, Y., and Wilson, A. G., "Prediction of turbulence-cascade interaction noise using modal approach," *2018 AIAA/CEAS Aeroacoustics Conference*, 2018, p. 3781. URL https://doi.org/10.2514/6.2018-3781.

[53] Jurdic, V., Joseph, P., and Antoni, J., "Investigation of rotor wake turbulence through cyclostationary spectral analysis," *AIAA Journal*, Vol. 47, No. 9, 2009, pp. 2022–2030. URL https://doi.org/10.2514/1.36728.

[54] Kissner, C., Guérin, S., Seeler, P., Billson, M., Chaitanya, P., Carrasco Laraña, P., de Laborderie, H., François, B., Lefarth, K., Lewis, D., et al., "ACAT1 Benchmark of RANS-Informed Analytical Methods for Fan Broadband Noise Prediction—Part I—Influence of the RANS Simulation," *Acoustics*, Vol. 2, Multidisciplinary Digital Publishing Institute, 2020, pp. 539–578. URL https://doi.org/10.3390/acoustics2030029.

[55] Moinier, P., "Algorithm developments for an unstructured viscous flow solver," Ph.D. thesis, Oxford University Oxford, UK, 1999.

[56] Campobasso, M. S., and Giles, M. B., "Effects of flow instabilities on the linear analysis of turbomachinery aeroelasticity," *Journal of propulsion and power*, Vol. 19, No. 2, 2003, pp. 250–259. URL https://doi.org/10.2514/2.6106.

[57] Guérin, S., Kissner, C., Seeler, P., Blázquez, R., Carrasco Laraña, P., de Laborderie, H., Lewis, D., Chaitanya, P., Polacsek, C., and Thisse, J., "ACAT1 Benchmark of RANS-Informed Analytical Methods for Fan Broadband Noise Prediction: Part II—Influence of the Acoustic Models," *Acoustics*, Vol. 2, Multidisciplinary Digital Publishing Institute, 2020, pp. 617–649. URL https://doi.org/10.3390/acoustics2030033.

[58] Moinier, P., and Giles, M. B., "Eigenmode analysis for turbomachinery applications," *Journal of Propulsion and Power*, Vol. 21, No. 6, 2005, pp. 973–978. URL https://doi.org/10.2514/1.11000.

[59] Moinier, P., Giles, M. B., and Coupland, J., "Three-dimensional nonreflecting boundary conditions for swirling flow in turbomachinery," *Journal of Propulsion and Power*, Vol. 23, No. 5, 2007, pp. 981–986. URL https://doi.org/10.2514/1.22117.

[60] Giacche, D., Xu, L., Coupland, J., and Watson, A. G., "Comparison between postprocessing methods applied to rotor-stator-interaction tone-noise problems," *AIAA Journal*, Vol. 49, No. 6, 2011, pp. 1214–1229. URL https://doi.org/10.2514/1.J050523.

[61] Atassi, O. V., "Computing the sound power in non-uniform flow," *Journal of Sound and Vibration*, Vol. 266, No. 1, 2003, pp. 75–92. URL https://doi.org/10.1016/S0022-460X(02)01448-7.

[62] Smith, S., "Discrete frequency sound generation in axial flow turbomachines," Tech. rep., Reports and memoranda, Aeronautical Research Control Council, 1972.

[63] Goldstein, M. E., *Aeroacoustics*, McGraw-Hill International Book Company, New York, 1976.